SIMULATION METHODOLOGIES

FOR SATELLITE SOLAR ARRAY DYNAMICS

A Thesis

by

NAVID MOHSENIZADEH

Submitted to the Office of Graduate Studies of
Texas A&M University
in partial fulfillment of the requirements for the degree of

MASTER OF SCIENCE

August 2010

Major Subject: Mechanical Engineering

Simulation Methodologies for

Satellite Solar Array Dynamics

SIMULATION METHODOLOGIES

FOR SATELLITE SOLAR ARRAY DYNAMICS

A Thesis

by

NAVID MOHSENIZADEH

Submitted to the Office of Graduate Studies of
Texas A&M University
in partial fulfillment of the requirements for the degree of

MASTER OF SCIENCE

Approved by:

Chair of Committee,	Alan Palazzolo
Committee Members,	Michael Schuller
	Bryan Rasmussen
Head of Department,	Dennis L. O'Neal

August 2010

Major Subject: Mechanical Engineering

ABSTRACT

Simulation Methodologies for Satellite Solar Array Dynamics. (August 2010)

Navid Mohsenizadeh, B.S., Shiraz University

Chair of Advisory Committee: Dr. Alan Palazzolo

The purpose of the present thesis is to furnish diverse studies on the dynamic response of satellite solar arrays. The term flexible structure or, briefly, structure has different interpretations and definitions, depending on source and on application. The solar array studied in the present thesis has flexible sub-structures and undergoes large deformations.

Structural dynamics is an important basis of many engineering studies associated with engineering structures, such as design, construction, and control. It generally consists of two functions, i.e. free vibration analysis (modal analysis) and response analysis (steady-state and transient analysis).

The thesis starts with introducing the solar array considered for our study and then continues with several structural analyses, including nonlinear pre-stressed static analysis, pre-stressed modal analysis, nonlinear full transient analysis and Fast Fourier Transform study on the transient response.

The purpose of static analysis is to obtain the configuration of the array under implementing static loads. Modal analysis provides the natural frequencies and mode shapes which are the intrinsic dynamic properties of the structure. Transient analysis is

used for evaluating the mechanical behavior of the structure. It gives relations between the intrinsic properties of structure and the external excitations. Transient analysis under different types of inputs will be used to track physical quantities like displacement, rotation, stress, and strain during specific satellite maneuvers. Pointing error will be introduced as a measure of accuracy of Sun tracking maneuver. It will be computed as a postprocessing step on the transient displacement results. To improve the pointing error which will consequently result in higher energy generating performance, two other staggering type input profiles are proposed for each orbit, GEO and LEO. Pointing error and vibration response under the proposed inputs are obtained to determine the efficiency of the new inputs. After a comparison, it will be shown that the proposed inputs are more efficient in the Sun tracking solar array maneuver.

At the end, a novel approach in performing mode-superposition transient analysis using modal effective mass tables is introduced. Since it is very common among engineers to assume the first 10% or 20% of the mode shapes when mode-superposition method is preferred to obtain the transient response, this novel approach shows that even smaller numbers of mode shapes can be assumed to perform this type of analysis and still obtain acceptable results, only if the assumed modes contain the majority of the modal effective mass in a specific direction, depending on the loading condition.

DEDICATION

To my mother,

my father

and

my brother

without their love, support and patience

my education would not be successful

ACKNOWLEDGEMENTS

I would like to thank my committee chair, Dr. Palazzolo, and my committee members, Dr. Schuller and Dr. Rasmussen, for their guidance and support throughout the course of this research and my academic pursuit.

Thanks also to Ray Stribling, Christian Dommell and Steven Bullock from Boeing Space & Intelligence Systems for making my time on their research a great experience. I also want to thank Christian Dommell for his valuable comments on my thesis.

I am grateful to Dr. Michael Beladi for his outstanding mentorship and continuous support. I am learning a lot from him in many aspects of life.

Thanks also to my mother, father and brother for their encouragement, patience and love.

Finally, I would like to thank everybody who was important to the successful realization of my education, as well as expressing my apology that I could not mention personally one by one.

TABLE OF CONTENTS

Page

ABSTRACT iii

DEDICATION v

ACKNOWLEDGEMENTS vi

TABLE OF CONTENTS vii

LIST OF FIGURES ix

LIST OF TABLES xiii

1. INTRODUCTION 1

    1.1 Satellites 1
    1.2 FAST Satellite Project 3
    1.3 Novel Contribution 4
    1.4 Practical Significance 5
    1.5 Literature Review 5

2. MODEL DESCRIPTION AND FINITE ELEMENT 8

    2.1 DARPA FAST Solar Array 8
    2.2 ANSYS Finite Element Model 12
    2.3 Deployment Studies 13
    2.4 Meshing the Solid Model 14

3. NONLINEAR PRE-STRESSED STATIC ANALYSIS AND STATIC CONFIGURATION 15

    3.1 Introduction 15
    3.2 Initial Strains and Static Loads 15
    3.3 Geometric Nonlinearity 16
    3.4 Boundary Conditions 16
    3.5 Nonlinear Pre-stressed Static Analysis Results 16

4. PRE-STRESSED MODAL ANALYSIS 18

Page

4.1 Introduction....18
4.2 Modal Effective Mass....19
4.3 Modal Analysis Results of a Single MCA....26
4.4 Pre-stressed Modal Analysis Results of the Solar Array....27
4.5 Elemental Strain Energy....30

5. HIGHLY ACCURATE SINGLE DOF EQUIVALENT MODEL OF COMPLEX SOLAR ARRAY....32

5.1 Motivation....32
5.2 Highly Accurate SDOF Equivalent Model for the First Mode....32
5.3 Highly Accurate SDOF Equivalent Model for the Third Mode....34

6. FULL NONLINEAR TRANSIENT ANALYSIS AND POINTING ERROR....38

6.1 Introduction....38
6.2 Array-Level Pointing Error....39
6.3 Transient Analysis under Solar Wing Drive (SWD) in GEO Orbit....42
6.4 Pointing Error Calculations for the Solar Array under SWD GEO....50
6.5 Improving Pointing Error by Exploring Different Staggering Type Inputs for the SWD GEO....52
6.6 Transient Analysis under Solar Wing Drive (SWD) in LEO Orbit....58
6.7 Pointing Error Calculations for the Solar Array under SWD LEO....61
6.8 Improving Pointing Error by Exploring Different Staggering Type Inputs for the SWD LEO....62

7. A NOVEL METHOD IN PERFORMING MODE-SUPERPOSITION TRANSIENT ANALYSIS USING MODAL EFFECTIVE MASSES....68

7.1 Motivation....68
7.2 Modal Analysis....70
7.3 Transient Analysis under Full and Mode-superposition Methods....71

8. CONCLUSION....74

REFERENCES....75

APPENDIX A ANSYS ELEMENT DESCRIPTION....80

VITA....85

LIST OF FIGURES

Page

Figure 1.1 Orbits around the Earth 2

Figure 1.2 A Satellite with Two Wings and a Bus at the Center 2

Figure 2.1 A Single MCA 8

Figure 2.2 Truss Link 9

Figure 2.3 Schematic of a Storable Tubular Extendible Member (STEM™) 10

Figure 2.4 DARPA FAST Solar Array 12

Figure 2.5 Finite Element Model of DARPA FAST Solar Array 12

Figure 2.6 Array-level Picture 13

Figure 3.1 Displacement Contour of the Solar Array after Static Analysis 17

Figure 4.1 Simple 3-Beam Frame in ANSYS (Left) and MATLAB (Right) 22

Figure 4.2 Simplified MCA 26

Figure 4.3 First Mode Shape for One of the Possible Design Configurations 28

Figure 4.4 Second Mode Shape for One of the Possible Design Configurations 29

Figure 4.5 Third Mode Shape for One of the Possible Design Configurations 29

Figure 4.6 Elements with More than 0.04% of Total SE in 3rd Mode 30

Figure 4.7 Elements with More than 0.1% of Total SE in 3rd Mode 31

Figure 4.8 Elements with More than 0.35% of Total SE in 3rd Mode 31

Figure 5.1 Definition of Physical Coordinate for the Equivalent Model 35

Page

Figure 5.2 Natural Frequency Comparison between Actual Solar Array and the Equivalent Model....37

Figure 6.1 MCAs Local Frames....40

Figure 6.2 Definition of Pointing Error 1....40

Figure 6.3 Definition of Pointing Error 2....41

Figure 6.4 Definition of Pointing Error 3....41

Figure 6.5 Rigid Location of a Specific Node....43

Figure 6.6 Total Location of a Specific Node....44

Figure 6.7 Flexible Displacement of a Specific Node in the Global Frame....44

Figure 6.8 Flexible Displacement of a Specific Node in the Local Rotating Frame....45

Figure 6.9 Flexible Displacement of a Specific Node under SWD GEO....46

Figure 6.10 Steady State Flexible Displacement of a Specific Node under SWD GEO....46

Figure 6.11 Steady State Transient Response of a Specific Node under SWD GEO....47

Figure 6.12 Frequency Spectrum for the Transient Response of a Specific Node under SWD GEO....48

Figure 6.13 One of the Array Mode Shape Participating with a Large Factor in the Transient Response....49

Figure 6.14 One of the Array Mode Shapes Participating with a Relatively Considerable Factor in the Transient Response....49

Figure 6.15 One of the Array Mode Shapes Participating with a Small Factor in the Transient Response....50

Figure 6.16 Error Sum for a Specified MCA under SWD GEO....51

Figure 6.17 Error Sum for another Specified MCA under SWD GEO....51

Page

Figure 6.18 Maximum Instantaneous Error Sum over All MCAs under SWD GEO 52

Figure 6.19 Transient Response under Different Inputs for SWD GEO 54

Figure 6.20 Transient Response (Left) and FFT (Right) Graphs for 9.6-9.6-periods Input for SWD GEO 55

Figure 6.21 Transient Response (Left) and FFT (Right) Graphs for 14.4-4.8-periods Input for SWD GEO 55

Figure 6.22 Transient Response (Left) and FFT (Right) Graphs for 4.8-4.8-periods Input for SWD GEO 56

Figure 6.23 Maximum Instantaneous Error Sum under Different SWD GEO Inputs 57

Figure 6.24 Transient Response of a Specific Node under SWD LEO in the LRF 58

Figure 6.25 Steady State Flexible Displacement of a Specific Node under SWD GEO in the LRF 59

Figure 6.26 Steady State Flexible Displacement of a Specific Node under SWD LEO for FFT Study 60

Figure 6.27 Frequency Spectrum Plot for the Flexible Displacement of a Specific Node under SWD GEO 61

Figure 6.28 Maximum Instantaneous Error Sum over All MCAs under SWD LEO 62

Figure 6.29 Transient Response under Different Inputs for SWD LEO 64

Figure 6.30 Transient Response (Left) and FFT (Right) Graphs for 0.4-0.4-periods Input for SWD LEO 65

Figure 6.31 Transient Response (Left) and FFT (Right) Graphs for 0.6-0.2-periods Input for SWD LEO 65

Figure 6.32 Transient Response (Left) and FFT (Right) Graphs for 0.2-0.2-periods Input for SWD LEO 66

Figure 6.33 Maximum Instantaneous Error Sum under Different SWD GEO Inputs 67

Page

Figure 7.1 Triangular Lattice Space Structure for Mode-superposition Transient Studies 69

Figure 7.2 Comparison of Full and Mode-superposition Methods 72

LIST OF TABLES

Page

Table 4.1 Dimensions and Material Properties of the Simple 3-Beam Frame.....22

Table 4.2 Natural Freq Comparison between ANSYS and MATLAB for the Simple 3-Beam Frame 23

Table 4.3 Modal Effective Mass Comparison between ANSYS and MATLAB for the Simple 3-Beam Frame 24

Table 4.4 Natural Frequencies and Modal Effective Masses of the Simple 3-Beam Frame Obtained in ANSYS.....25

Table 5.1 MCA Model vs. Equivalent Simple String Model.....33

Table 6.1 Summary of FFT Results for All SWD GEO Input Cases.....56

Table 6.2 Summary of FFT Results for All SWD GEO Input Cases.....66

Table 7.1 Modal Analysis Results of the Lattice Space Structure under Study.....70

1. INTRODUCTION

1.1 Satellites

A satellite is an object which has been placed into orbit by human endeavor. Satellites can be categorized into different types based on their missions. Some of these types are summarized as follows:

- Astronomical Satellites are used for observation of distant planets, galaxies and other outer space objects.
- Communication Satellites are used with the purpose of telecommunications.
- Navigational Satellites use radio time signals transmitted to enable mobile receivers on the ground to determine their exact location.
- Weather Satellites are primarily used to monitor Earth's weather and climate.

The commonly used altitude classifications for satellites are:

- Low Earth Orbit (LEO), orbits below 2000km
- Medium Earth Orbit (MEO), higher than 2000km but still below the altitude for geosynchronous orbit (GEO) at 35786 km
- Geosynchronous Earth Orbit (GEO), which is at the altitude of 35786 km.
- High Earth Orbit (HEO), higher than the altitude for geosynchronous orbit (GEO)

This thesis follows the style of *IEEE Journal of Automatic Control*.

The following picture shows a schematic of the orbits around the Earth used for satellites.

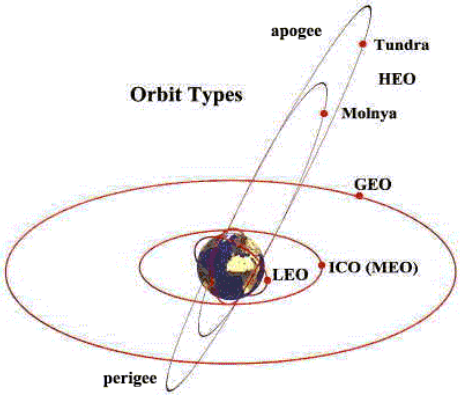

Figure 1.1 Orbits around the Earth

The following picture is showing a satellite that has a solar array, comprised of two solar wings and a bus at the center.

Figure 1.2 A Satellite with Two Wings and a Bus at the Center

Satellites can have fewer or more wings depending on their missions and designs. Most satellite solar arrays consist of solar cells mounted on a rigid substrate (e.g. honeycomb panels). However, since the 1970s, flexible solar panels and lightweight deployable systems have been deployed for specialized applications. Numerous studies on solar arrays and space structures have been conducted so far. Junkins *et. al.* presents methodologies of dynamics of flexible structures in [1], [2]. Kirk *et. al.* in [3], [4] and Wie in [5], [6] conduct several researches on dynamics and control of structures in space. Kirk *et. al.* perform diverse dynamics of structures in [7], [8]. Dynamics of space tether systems is conducted by Beletsky and Levin in [9]. Studies of large space structures expanded by centrifugal forces are performed in [10]. Studies on control of large flexible space structures (LFSS) in [11]- [12] presents some developed controller synthesis methods.

1.2 FAST Satellite Project

Fast Access Spacecraft Testbed (FAST) project aims to develop a High Power Generation Subsystem (HPGS) that can be readily integrated with current high power spacecraft and with the next generation of compact and highly maneuverable spacecraft to provide power for both payload and propulsion purposes. Some especial features and innovations of the project are as follows:

- Very high specific power (>130 watts/kg).
- Very similar ultra-lightweight, ultra-stiff, structural/deployment concept has already been ground tested.

- Uses next generation 33% efficient IMM solar cells.
- No active cooling system.
- It is exceptionally radiation hard for survivability to natural and unnatural radiation threats.

1.3 Novel Contribution

Solar arrays are complex flexible structures; therefore, exploring different approaches in methodologies of dynamics of these structures can lead to further progress and introduce a new era in dynamical studies of solar arrays.

The present thesis introduces a number of methods, simplified models and improvements that are obtained as a result of the dynamical studies and simulations performed on solar arrays. Major accomplishments presented in the thesis can be summarized as:

- Introducing two highly accurate single DOF equivalent models for the first translational and rotational mode shapes
- Proposing new input profiles for SWD (Solar Wing Drive) maneuver in GEO and LEO orbits that exceptionally decrease the pointing error and vibrations amplitude
- Presenting a novel method in performing mode-superposition transient analysis using modal effective mass results

1.4 Practical Significance

The proposed methods and approaches contribute to higher solar array dynamic performance. The practical significance aspects of the accomplishments presented in the thesis can be abstracted, but not limited, to:

- The novel equivalent single DOF models can be used in parametric studies and estimating the natural frequencies of specific modes under different tension loads in Tension Wires.
- The new proposed input profiles for SWD in GEO and LEO orbits exceptionally decrease the pointing error by 66% and 84% respectively. This contributes to higher energy generating performance of the solar array.
- The new method of performing mode-superposition transient analysis explains that a smaller number of mode shapes, compared to the common method of assuming first 10% or 20% of the mode shapes, can be assumed if the considered mode shapes cover a large amount of modal effective mass. This decreases the volume of calculations and required processing time for obtaining the transient response when mode-superposition approach is preferred.

1.5 Literature Review

The solar array studied in the present thesis is a flexible space structure that undergoes large deformations. This geometric nonlinearity effect is considered in the studies and analyses preformed. Significant portion of the results have been removed due to proprietary restrictions on Boeing and DR Technologies data.

Section 1 summarizes the objectives and accomplishments obtained in this thesis through studies and simulations performed on the solar array dynamics.

Section 2 introduces the DARPA FAST solar array studied in the current thesis. The sources and journal publications that have been studied to acquire theoretical and practical backgrounds for further structural analyses are cited in this section.

Section 3 presents the results of nonlinear pre-stressed static analysis. The final static configuration will be showed.

Section 4 introduces the modal effective mass concept as a measure to classify the importance of a mode shape. The array mode shapes will be shown in this section. Elemental strain energy contour for a specific mode shape of the array is plotted to identify the locations where the most of the strain energy corresponds to that mode is stored.

Section 5 proposes two highly accurate single DOF equivalent models for the first translational and rotational mode shapes of the solar array. The equivalent model for the first rotational mode is used to estimate the natural frequency of the array under different tension loads. The results of the equivalent models are compared to the actual complex array model to determine the efficacy of the proposed SDOF models.

Section 6 is devoted to transient analyses in GEO and LEO orbits. Pointing error is introduced and the corresponding calculations are performed on the transient response of the array as a postprocessing step. The proposed input profiles for SWD (Solar Wing Drive) maneuver in GEO and LEO orbits are introduced in this section. Vibrations response, results of Fast Fourier Transform study and pointing error calculations under

the new proposed inputs will be compared to the results under current design to determine the efficacy of the proposed input profiles.

Finally, section 7 presents a novel method in obtaining transient response using mode-superposition method. Modal effective mass results can be used to determine the required number of mode shapes for performing mode-superposition transient analysis. A large flexible triangular lattice space structure is modeled and transient analysis is performed using full method, mode-superposition methods assuming first 10% and first 1% of the total mode shapes extracted in the modal analysis. Results confirm that the transient response will be valid regardless of the number of assumed mode shapes as far as the assumed mode shapes cover a large amount of modal effective mass in directions that depend on the loading conditions.

2. MODEL DESCRIPTION AND FINITE ELEMENT

2.1 DARPA FAST Solar Array

DARPA FAST array, developed by Boeing Space & Intelligence Systems, is made up of linear concentrator elements held in a tensioned array. Major subsystems of this array are as follows:

1) **Linear Concentrator / Multifunctional Concentrator Assembly (MCA)**

MCAs are curved-shape mirrors. A single MCA is shown below.

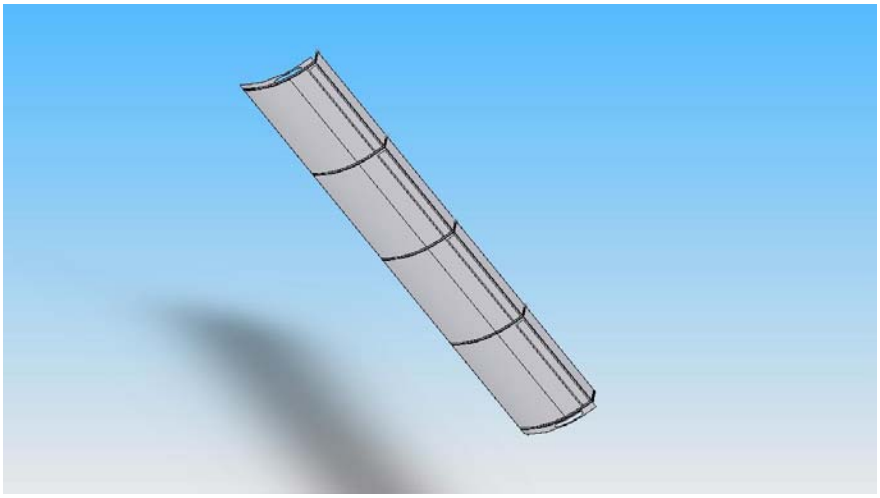

Figure 2.1 A Single MCA

2) **Truss Link**

Truss Links connect MCAs together. The following picture shows a number of MCAs connected with Truss Links and Tension Wires.

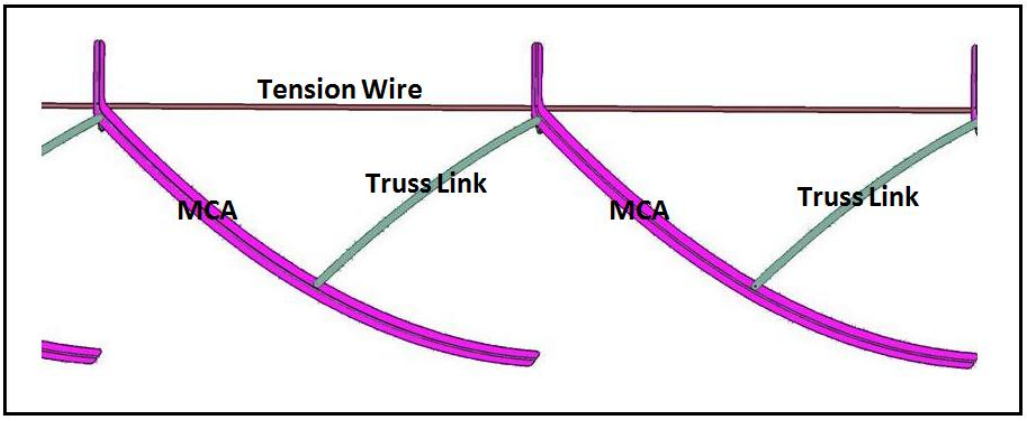

Figure 2.2 Truss Link

3) Tension Wire

Tension Wires are responsible for providing tension force between MCAs. A part of Tension Wire between two MCAs is shown in the above picture. This force keeps all the MCAs tight together and with the aid of Truss Links prevents unwanted relative motion of MCAs. Therefore, in some sense, this force controls the relative motions between MCAs and as it is shown later can change the dynamic behavior of the structure.

4) Storable Tubular Extendible Member (STEM™) or Bow Spring/Beam

STEM™ is a trademark developed by Northrop Grumman Astro-Aerospace Corporation. Extendible spacecraft booms deploy spacecraft subsystems including sensitive instruments, provide inertial configurations required for gravity-gradient (GG) attitude control, and serve as lightweight antennas in orbit and during recovery for both spacecraft and surrounding rocket type applications [13].

Solar-radiation, magnetic, gravitational and atmospheric drag forces have a significant effect upon the design of spacecraft booms, may degrade communication system performance, attitude control accuracy and stability, and instrument experimental data [13]. Satellite with long extendible appendages of open cross section have experienced unstable oscillations. The problem of torsional instability in extendible booms with open cross sections is studied in [14]. Timoshenko develops the theory of elastic stability in [15]. Stability and buckling studies on continues structures are provided by Como *et. al.* in [16]. An analytical approach for determining the thermal-structural response of a flexible roll-up solar array due to a sudden increase in external heating is developed in [17].

Bow Springs provide the outward spring force required to put the Tension Wires and Tethers in tension. Tension is critical to the stability of the entire system.

The following picture shows a schematic of a STEM™.

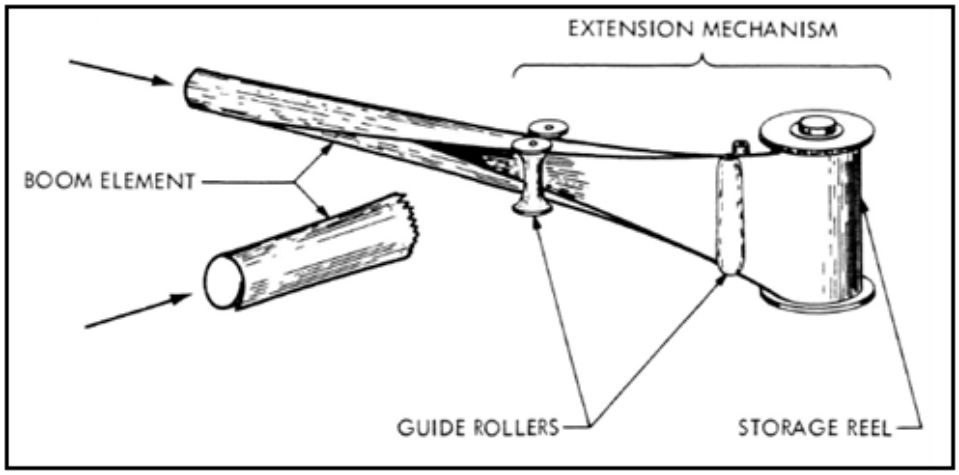

Figure 2.3 Schematic of a Storable Tubular Extendible Member (STEM™)

Since Bow Spring has an open section, a study on open-section beams should be conducted for a better understanding of the possible phenomena that may happen to the Bow Springs during and after deployment. Gupta and Rao developed finite element analysis to study instability of then-walled open-section laminated composite beams in [18], [19]. Megson studies shear and torsion in thin-walled open-section beams in [20].

Bow Spring cross section inertias I_{yy} and I_{zz} can be calculated from the equations provided in [21].

5) **End Beam**

End Beam spans between the Bow Beams from the End Housing.

6) **Tether**

Tethers are long cables that span end of the Tether Beams to the end of the End Beam.

7) **Yoke**

Yoke is a beam-like arm that attaches the solar array to the BUS. Any solar array maneuver and motion control of the array, like Solar Wing Drive (SWD), Solar Wing Positioning (SWP) are implemented using the Yoke as the driving arm.

The following picture, presented in Boeing's Space Power Workshop - April 2010, shows the DARPA FAST array assembled on a bus.

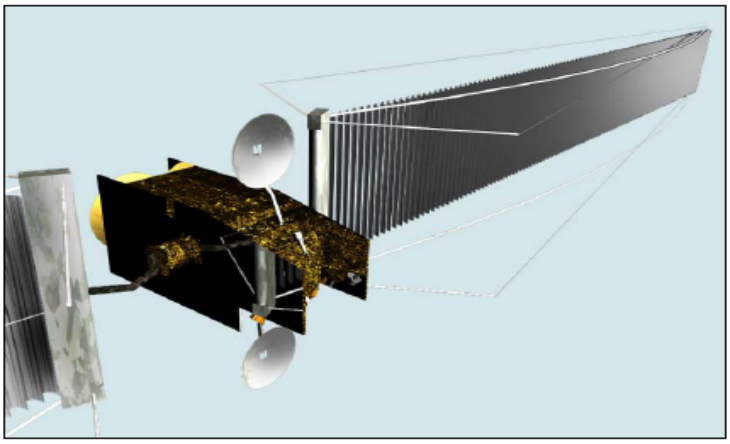

Figure 2.4 DARPA FAST Solar Array

2.2 ANSYS Finite Element Model

The following picture is showing the deployed model of the FAST Satellite solar array generated in ANSYS finite element software.

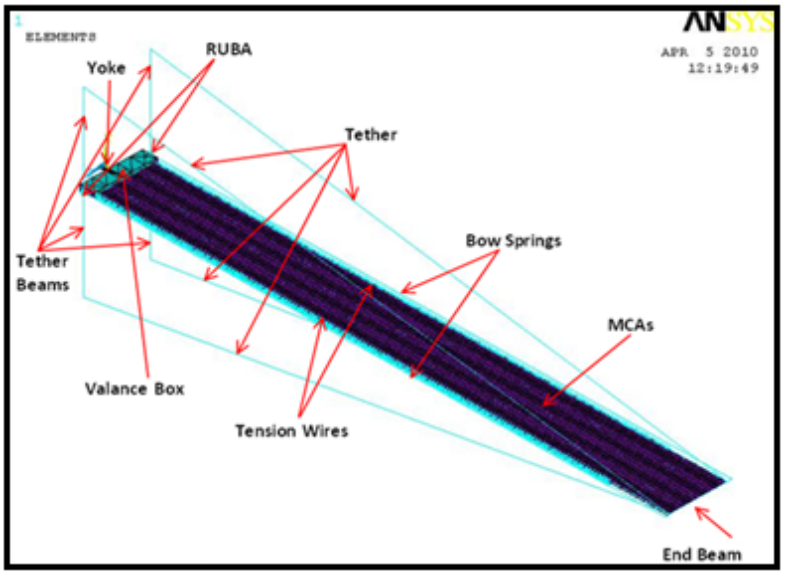

Figure 2.5 Finite Element Model of DARPA FAST Solar Array

The following picture shows a close view of a number of MCAs connected together with Truss Links and Tension Wires.

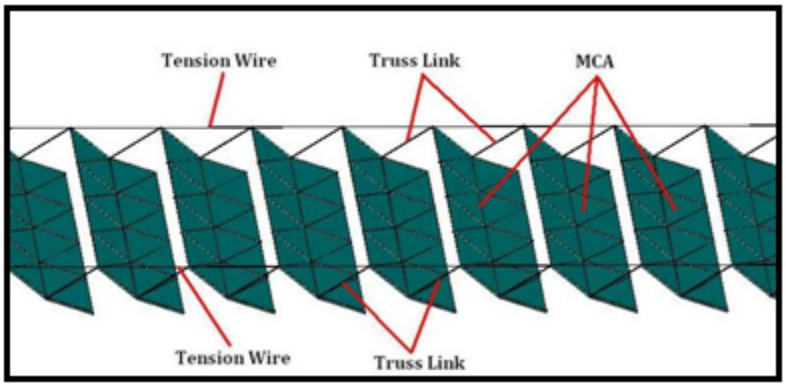

Figure 2.6 Array-level Picture

2.3 Deployment Studies

Analysis on the dynamic characteristic of the deployment mechanism must be done at an initial design stage. Some dynamic analyses to predict solar panel deployment motions are proposed in [22]. Many researchers have simulated the deployment of flexible solar arrays. Wallrapp and Wiedemann simulated a 3D deployment of a flexible solar array in SIMPACK (multi-body simulation software) in [23], [24].

2.4 Meshing the Solid Model

After generating geometry of the model, the material properties, element types and cross sections should be defined for each component. ANSYS has a wide variety of element types for performing structural, thermal, electromagnetic and other types of analyses. It also has the capability to perform coupled analyses, like coupled thermal-structural analyses.

Description of some widely used elements are provided in 0. Selection of an element type needs a thorough understanding of the capabilities of that element, some experience and may need consulting other experts.

3. NONLINEAR PRE-STRESSED STATIC ANALYSIS AND STATIC CONFIGURATION

3.1 Introduction

This section presents the results of nonlinear pre-stressed static analysis. The purpose of this analysis is to find the static tension or compression loads, stress distribution profile and displacements occurring within the array structure. Since the array undergoes large deformations, this forces the problem to be geometrically nonlinear.

3.2 Initial Strains and Static Loads

Tension in Tethers and Tension Wires is applied by introducing initial strain for the elements used to model these components. Calculating the tension load for Tethers and Tension Wires is a part of the design process where several criteria are to be considered. These tension loads can be found from the geometry of the array structure and material properties of these components. The required tension load for Tension Wires is provided by the sub-system designers.

Having the tension loads we are able to apply initial strains and perform the static analysis. Initial strains are calculated as follows:

$$\begin{cases} F = kx \\ k = \dfrac{EA}{L} \end{cases} \implies FL = EAx \implies \delta(strain) = \frac{x}{L} = \frac{F}{EA}$$

where *L* is the length of the string, Tether or Tension Wire. In the case of Tension Wire *L* is the distance between two adjacent MCAs.

3.3 Geometric Nonlinearity

In general, nonlinearity in structural mechanics can arise in many different ways. Problems involving deformations that are large are called geometrically nonlinear problems [25]. The studied solar array undergoes large deformations which force the problem to be categorized as geometrically nonlinear. The theory and computer implementation of the finite element methods applicable to simple problems of solid mechanics, fluid mechanics, and heat transfer are studied in [26], [27]. Vo and Lee have conducted several approaches on geometrically nonlinear analysis of thin-walled open-section composite beams in [28], [29], [30].

3.4 Boundary Conditions

As discussed before, solar array maneuvers are performed using the Yoke as the driving arm. Therefore all relative motions in array-level can be referenced to the Yoke. In the static analysis all degrees of freedom at the end of the Yoke will be set to zero.

3.5 Nonlinear Pre-stressed Static Analysis Results

The following picture shows the static configuration of the solar array after performing static analysis.

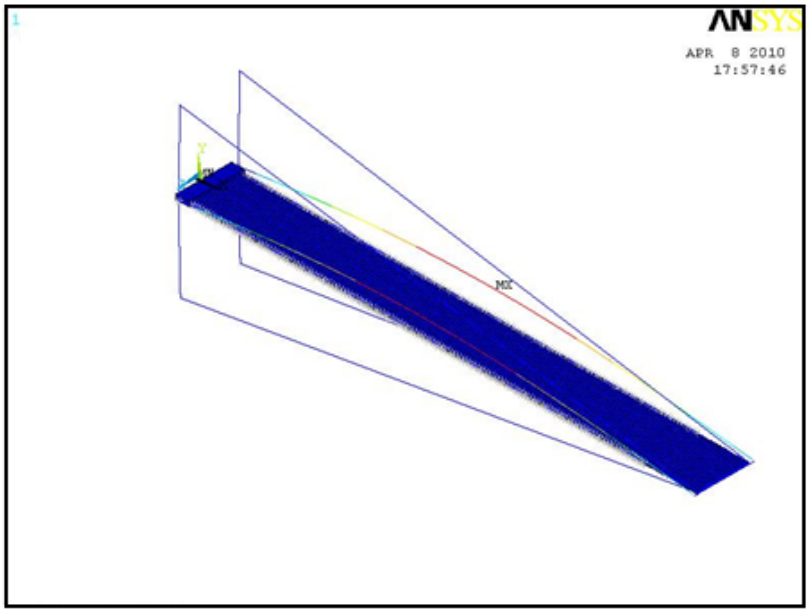

Figure 3.1 Displacement Contour of the Solar Array after Static Analysis

The obtained chord height in Bow Springs meets the design requirement. This chord height is the optimal design parameter which stabilizes the array dynamics and is calculated from parametric studies performed on the actual equipment, Bow Spring, and computer finite element model.

The static loads in different components, stress and strain profiles can be obtained for further considerations.

4. PRE-STRESSED MODAL ANALYSIS

4.1 Introduction

Modal analysis is the study of the dynamical behavior of structures under vibrational excitations. It provides natural frequencies and mode shapes (geometric configurations) of the structure. Any arbitrary response of the system can be interpreted as a linear combination of these modal vibrations, and as a result its analysis may be conveniently done using modal analysis techniques. It is an important tool in the analysis, diagnosis, design, and control of vibration. By modal analysis it is possible to establish the extent and locations of sever vibrations in a system [31]. The mode shapes obtained from modal analysis can be used to perform mode superposition transient analysis where the number of degrees of freedom of a structure is reduced to the number of assumed modes resulting in a faster processing to obtain the transient response.

This section introduces the concept of modal effective mass and its importance in characterizing the dynamical response of a structure through the modal simulation of a simple 3-beam truss model. The results obtained from pre-stressed modal analysis on the solar array including natural frequencies, mode shapes, and modal effective masses are provided in this section.

Since the MCAs are simplified from their original complex structure for the purpose of generating the deployed model at the array level, a separate modal analysis is performed on a single simplified MCA to compare the results of natural frequencies and mode shapes to the original one.

4.2 Modal Effective Mass

4.2.1 Concept and Definition

The modal effective mass is a modal dynamic property of a structure associated with the modal properties; natural frequencies, mode shapes, generalized masses and participation factors. The modal effective mass is a measure to classify the importance of a mode shape when the structure is excited by base acceleration. A high modal effective mass will lead to a high reaction force at the base [32].

The modal effective mass is a 6×6 mass matrix. Within this matrix the coupling between translations and rotations, for a certain mode shape, can be traced. Also the summation over all modal effective masses will result if the mass matrix as a rigid body [32].

For an M-DOF system the undamped equation of motion for a free-free elastic body can be written as

$$\begin{bmatrix} M_{ii} & M_{ij} \\ M_{ji} & M_{jj} \end{bmatrix} \begin{Bmatrix} \ddot{x}_i \\ \ddot{x}_j \end{Bmatrix} + \begin{bmatrix} K_{ii} & K_{ij} \\ K_{ji} & K_{jj} \end{bmatrix} \begin{Bmatrix} x_i \\ x_j \end{Bmatrix} = \begin{Bmatrix} F_i \\ F_j \end{Bmatrix} \qquad (4.2.1)$$

where the index j denotes the external or boundary degrees of freedom and the index i denotes the internal degrees of freedom [32].

The displacement vector [x(t)] can be written on a basis of 6 rigid-body modes $[\Phi_r]$ with $\{x_j\} = [I]$, $j \leq 6$ and elastic mode shapes $[\Phi_p]$ with fixed external degrees of freedom $\{x_j\} = \{0\}$ calculated from the eigenvalue problem

$$\left([K_{ii}] - \langle \lambda_p \rangle [M_{ii}]\right)[\Phi_{ii}] = [0] \qquad (4.2.2)$$

Therefore the displacement vector $\{x(t)\}$ can be written as

$$\{x\} = [\Phi_r]\{x_j\} + [\Phi_p]\{\eta_p\} = [\Phi_r \quad \Phi_p]\begin{Bmatrix} x_j \\ \eta_p \end{Bmatrix} = [\Psi]\{X\} \qquad (4.2.3)$$

where $\{\eta_p\}$ is the generalized coordinates and $[\Psi]$ is called the Craig-Bampton transformation matrix. In general, the number of generalized coordinates p is much less than the total number of degrees of freedom $n = i + j, p \ll i$.

By substituting the Craig-Bampton transformation into (4.2.1), it becomes

$$[\Psi]^T[M][\Psi]\{\ddot{X}\} + [\Psi]^T[K][\Psi]\{X\} = [\Psi]^T\{F(t)\} = \{f(t)\} \qquad (4.2.4)$$

and then

$$\begin{bmatrix} M_{rr} & M_{jp} \\ M_{pj} & m_p \end{bmatrix}\begin{Bmatrix} \ddot{x}_j \\ \ddot{\eta}_p \end{Bmatrix} + \begin{bmatrix} \widetilde{K}_{jj} & K_{jp} \\ K_{pj} & k_p \end{bmatrix}\begin{Bmatrix} x_j \\ \eta_p \end{Bmatrix} = \begin{bmatrix} \Phi_{ij} & \Phi_p \\ I & 0 \end{bmatrix}^T \begin{Bmatrix} F_i \\ F_j \end{Bmatrix} \qquad (4.2.5)$$

with

- $[M_{rr}]$ the 6×6 rigid body mass matrix with respect to the boundary DOFs
- $\left[\widetilde{K}_{jj}\right]$ the Guyan reduced stiffness matrix (j-set)
- $\langle m_p \rangle$ the diagonal matrix of generalized masses, $\langle m_p \rangle = \left[\Phi_p\right]^T[M]\left[\Phi_p\right]$
- $\langle k_p \rangle$ the diagonal matrix of generalized stiffnesses,

$$\langle k_p \rangle = \left[\Phi_p\right]^T[K]\left[\Phi_p\right] = \langle \lambda_p \rangle \langle m_p \rangle = \langle {\omega_p}^2 \rangle \langle m_p \rangle$$

- $\left[K_{ip}\right] = \left[\Phi_{ij}\right]^T[\mathrm{K}_{ii}]\left[\Phi_p\right] + \left[\mathrm{K}_{ji}\right]\left[\Phi_p\right] = \left(-\left[\mathrm{K}_{ij}\right]^T[\mathrm{K}_{ii}]^{-1}[\mathrm{K}_{ii}] + \left[\mathrm{K}_{ji}\right]\right)\left[\Phi_p\right] = [0]$
- $\left[K_{pi}\right] = \left[K_{ip}\right]^T = [0]$
- $\left[\widetilde{K}_{jj}\right] = [\Phi_r]^T[K][\Phi_r] = [0]$

Thus (4.2.5) becomes

$$\begin{bmatrix} M_{rr} & L^T \\ L & m_p \end{bmatrix} \begin{Bmatrix} \ddot{x}_j \\ \ddot{\eta}_p \end{Bmatrix} + \begin{bmatrix} 0 & 0 \\ 0 & m_p \lambda_p \end{bmatrix} \begin{Bmatrix} x_j \\ \eta_p \end{Bmatrix} = \begin{bmatrix} \Phi_{ij} & \Phi_p \\ I & 0 \end{bmatrix}^T \begin{Bmatrix} 0 \\ F_j \end{Bmatrix} = \begin{Bmatrix} F_j \\ 0 \end{Bmatrix} \quad (4.2.6)$$

where $[M_{jp}] = [\Phi_r]^T [M] [\Phi_p] = [L^T]$, $[L^T]$ is the matrix with the modal participation factors, $L_{kl} = \{\phi_{r,k}\}^T [M] \{\phi_{p,l}\}$, $k = 1,2,\dots,6$, $l = 1,2,\dots,p$.

The matrix of modal participation factors couples the rigid-body modes $[\Phi_r]$ with the elastic modes $[\Phi_p]$ and $\{F_i\} = \{0\}$, no internal loads are applied.

$[L_k] = \{\phi_{p,k}\}^T [M] [\Phi_r]$ is the 1×6 vector with modal participation factors.

It can be proved that [32]

$$[M_{rr}] = \sum_{k=1}^{p} \frac{[L_k]^T [L_k]}{m_k} \quad (4.2.7)$$

The modal effective mass $[M_{eff,k}]$ is defined as follows

$$[M_{eff,k}] = \frac{[L_k]^T [L_k]}{m_k} \quad (4.2.8)$$

where $m_k = \{\Phi_{p,k}\}^T [M] \{\Phi_{p,k}\}$, which is the k-th entry on the main diagonal of the modal mass matrix.

The summation over all modal effective masses $[M_{eff,k}]$ will result in the rigid-body mass matrix $[M_{rr}]$ with respect to $\{x_j\}$.

4.2.2 Calculation of Modal Effective Mass for a Simple 3-Beam Frame in MATLAB and ANSYS

Doyle studies modal analysis for frames with emphasize on computer matrix methods in [33]. A simple 3-beam truss is modeled in ANSYS and MATLAB in order

to determine the correlation between the results of the modal effective masses. Schiff provides natural frequencies of this simple 3-beam frame in [34] for in-plane and out-of-plane vibrations. ANSYS provides the modal effective masses in the result file from modal analysis; however, a code is generated in MATLAB based on the equations derived in the previous section for modal effective mass calculations.

The following picture is showing a simple 3-beam frame generated in ANSYS and MATLAB.

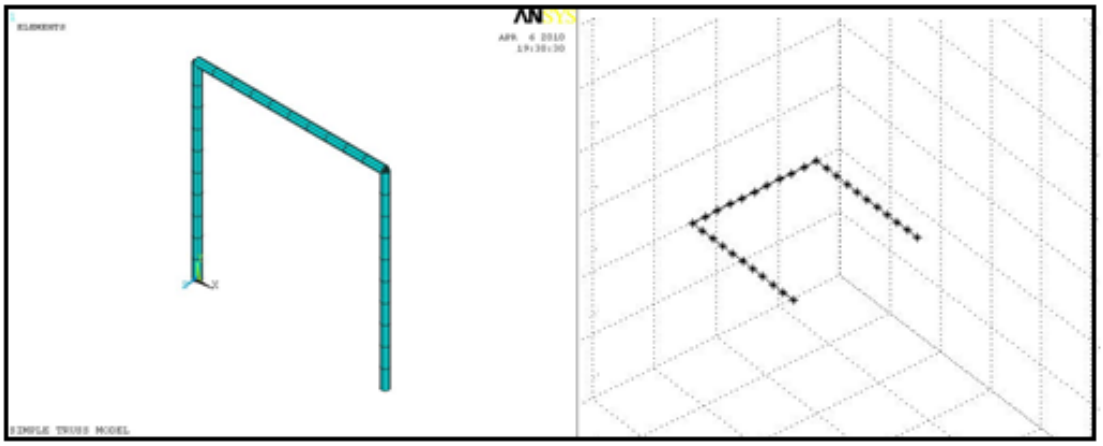

Figure 4.1 Simple 3-Beam Frame in ANSYS (Left) and MATLAB (Right)

Dimensions and material properties of the beams are given in the following table.

Table 4.1 Dimensions and Material Properties of the Simple 3-Beam Frame

Length [m]	Cross Section		Young's Modulus E [GPa]	Density [kg/m^3]	Poisson's Ration
	Ro [m]	Ri [m]			
1	0.03	0.02	70	2710	0.3

In both models each beam is meshed with 10 equal size elements and the ends of the vertical beams are grounded. Then a modal analysis is performed.

The following table summarizes the comparison between natural frequencies obtained for the first 20 modes from ANSYS and MATLAB for the simple 3-beam frame.

Table 4.2 Natural Freq Comparison between ANSYS and MATLAB for the Simple 3-Beam Frame

Mode	Freq [Hz]		% Error	Mode	Freq [Hz]		% Error
	ANSYS	MATLAB			ANSYS	MATLAB	
1	16	16	1	11	389	370	5
2	26	26	0	12	463	437	6
3	34	34	1	13	467	438	7
4	103	102	1	14	541	504	7
5	112	111	1	15	541	510	6
6	165	162	2	16	829	750	11
7	170	166	2	17	854	769	11
8	183	179	2	18	1011	896	13
9	189	185	2	19	1022	901	13
10	378	359	5	20	1024	915	12

As can be seen from the above table, the error between the natural frequencies obtained in ANSYS and MATLAB is less than 10% for modes under 800Hz.

Using equation (4.2.8) in MATLAB to calculate the modal effective masses and comparing the results with ANSYS result file revealed that the ANSYS output is strongly correlated with the cook-book formula utilized in MATLAB.

The following table is presenting a comparison between the modal effective masses obtained from ANSYS and MATLAB.

Table 4.3 Modal Effective Mass Comparison between ANSYS and MATLAB for the Simple 3-Beam Frame

Mode	Freq [Hz]	Modal Effective Mass			% Error
		Direction	ANSYS	MATLAB	
1	16	z	7.09	7.0855	0
2	26	x	7.64	7.6312	0
3	34	Not Significant			
4	102	y	1.81	1.8035	0
5	111	z	1.03	1.0273	0
6	162	Not Significant			
7	166	x	1.15	1.137	1
8	179	y	0.84	0.8277	1
9	185	z	0.69	0.6808	1
10	359	x	0.21	0.2072	1

As presented before, the summation over all modal effective masses will result in the rigid-body mass matrix. The output result from ANSYS shows the mass of structure as 10.01 kg and MATLAB calculates this quantity as 10.22 kg, which verifies the high level of accuracy of ANSYS results for modal effective masses.

For further modal analyses it is preferred to use percent modal effective mass rather than modal effective mass. Percent modal effective mass, for each mode and in each direction can be obtained by

$$Percent\ Modal\ Effective\ Mass|_{Mode\ i,\ \ Direction\ j}$$

$$= \frac{Modal\ Effecive\ Mass|_{Mode\ i,\ \ Direction\ j}}{Total\ Mass} \times 100$$

For instance, in the case of the simple truss model discussed before, the following table summarizes the results of the natural frequencies and percent modal effective masses for the first 20 modes obtained from ANSYS.

Table 4.4 Natural Frequencies and Modal Effective Masses of the Simple 3-Beam Frame Obtained in ANSYS

Mode	Freq [Hz]	%X	%Y	%Z	%ROTX	%ROTY	%ROTZ
1	16.16	0	0	70.85	98.01	39.94	0
2	25.97	76.3	0	0	0	0	55.21
3	34.42	0	0	0	0	30	0
4	103.25	0	18.06	0	0	0	4.47
5	112.31	0	0	10.25	1.33	5.78	0
6	165.46	0	0	0	0	6.74	0
7	169.61	11.47	0	0	0	0	0.42
8	183.44	0	8.41	0	0	0	2.08
9	188.74	0	0	6.9	0.5	3.89	0
10	377.51	2.13	0	0	0	0	1.29
11	388.77	0	0	0	0	1.24	0
12	463.28	0	0	4.66	0.14	2.63	0
13	467.29	0	0.07	0	0	0	0.02
14	540.97	0	0	0	0	1.75	0
15	541.05	3.24	0	0	0	0	1.46
16	829.06	0	12	0	0	0	2.97
17	853.96	0	0	1.17	0.02	0.66	0
18	1011.17	0	0	0	0	1.3	0
19	1021.83	0	0	1.39	0.02	0.78	0
20	1024.24	2.31	0	0	0	0	0.04
SUM		**95.45**	**38.54**	**95.21**	**100.02**	**94.7**	**67.96**

Results of natural frequencies and modal effective masses can be used for further optimal design steps. Sergeyev *et. al.* provide a method in determining the optimal joint positions and cross section parameters of linear elastic space frames with imposed stress and free frequency constraints in [35].

4.3 Modal Analysis Results of a Single MCA

MCAs are composed of many parts making them complicated for transient analyses. Therefore they are simplified into simple curved-profile shells and meshed using SHELL93 elements. The following picture is showing a single simplified MCA modeled and meshed in ANSYS.

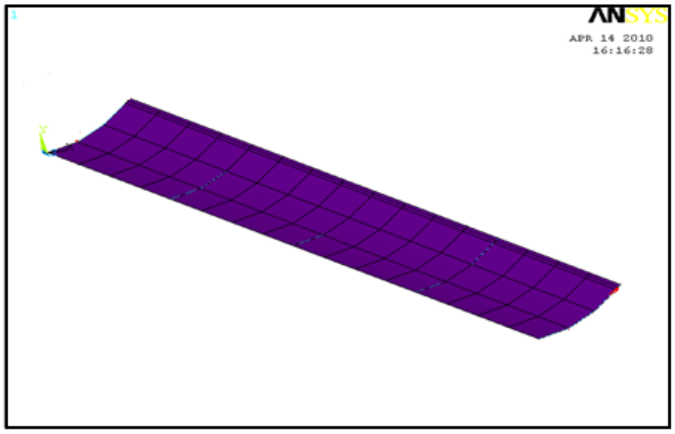

Figure 4.2 Simplified MCA

To compare the natural frequencies and mode shapes of the simplified MCA with the original one, a modal analysis is performed on a single MCA.

Since each MCA is in contact with Truss Links at four points, the boundary condition is applied by setting the DOF at those four points equal to zero.

The first mode natural frequency of this simplified model obtained the same as the actual complex model and the second natural frequency obtained with 8% error. Therefore, the results obtained for the simplified model is in a good agreement with the results that designers have for the complex model of MCAs. This also confirms that the simplified MCAs can be used for the array for further analyses and dynamical studies.

4.4 Pre-stressed Modal Analysis Results of the Solar Array

After performing the pre-stressed nonlinear static analysis, a pre-stressed modal analysis on the FAST solar array assuming 500 modes is done. The results obtained from this analysis are widely used for designing solar array maneuvers and dynamical studies. The following picture is showing the first mode shape for one of the possible design configurations for FAST. This is an out-of-plane bending motion of the array. An amplification factor of 30 is used for the following mode shape picture.

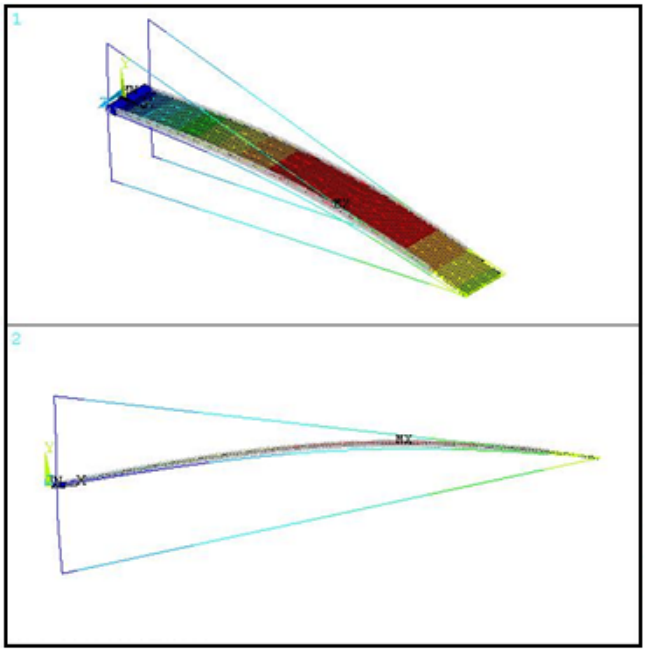

Figure 4.3 First Mode Shape for One of the Possible Design Configurations

The following two pictures are showing the second and the third mode shapes for one of the possible design configurations of the FAST solar array. The left-hand side picture is an in-plane motion of MCAs and the right-hand side picture is the rotation of the array about its longitudinal axis.

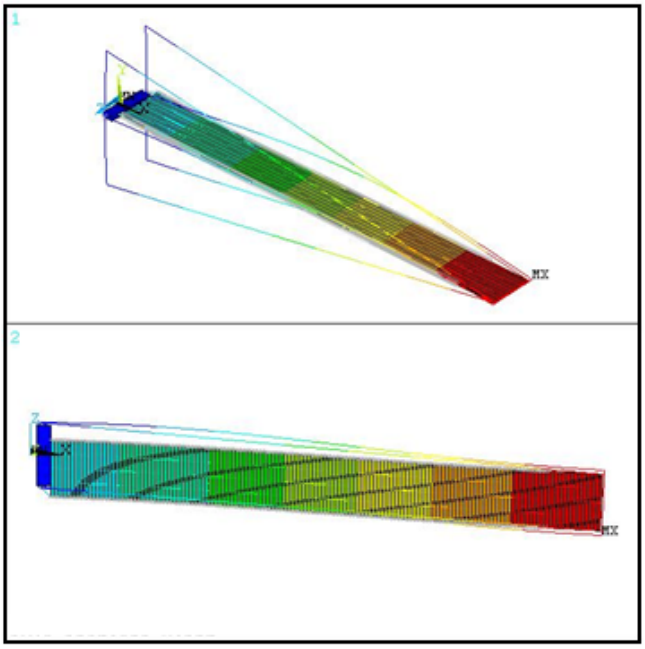

Figure 4.4 Second Mode Shape for One of the Possible Design Configurations

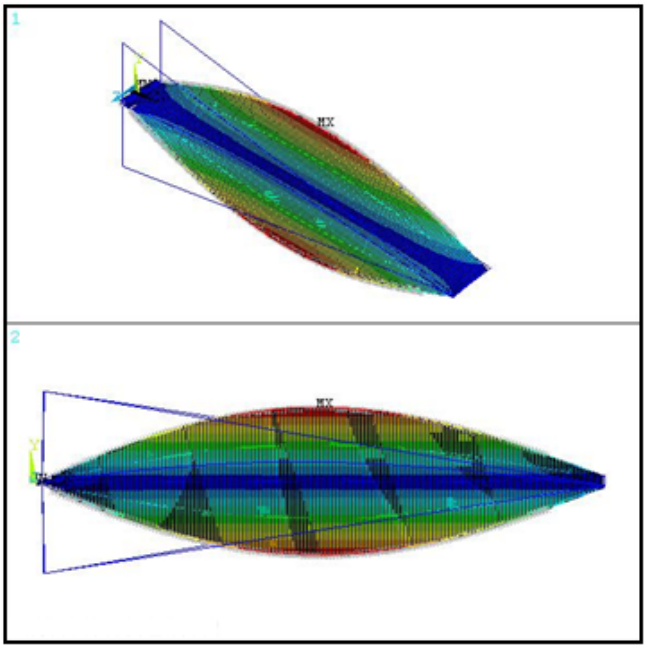

Figure 4.5 Third Mode Shape for One of the Possible Design Configurations

4.5 Elemental Strain Energy

Strain energy is referred to the energy stored in an elastic solid when it is deformed under load. Strain energy contour plot is a powerful tool in determining the locations where the material stores most of the total strain energy in that specific configuration. Elements storing the majority of strain energy, if needed, can be fortified to avoid possible future failures.

Strain energy contour plots are plotted for the 3rd mode to determine the locations storing most of the total strain energy of this mode. Total strain energy of this mode can be obtained by summing up the strain energy of all elements. Then each element's strain energy will be divided by the total to find the percent strain energy of that specific element. The following picture shows the elements within the solar array having more than 0.04% of the total strain energy in the 3rd mode.

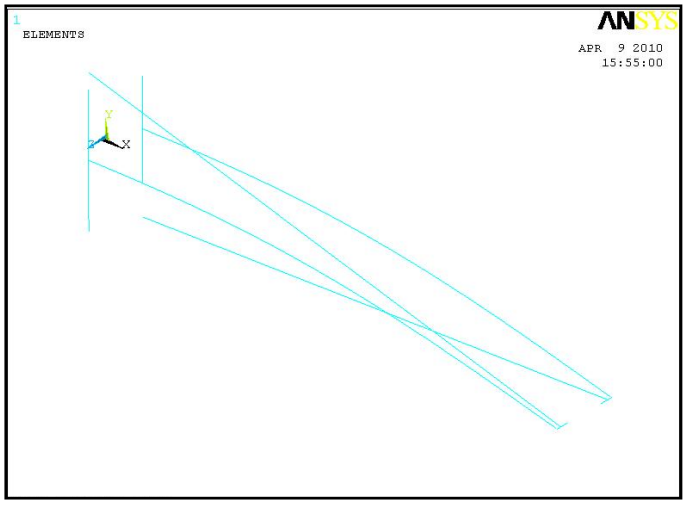

Figure 4.6 Elements with More than 0.04% of Total SE in 3rd Mode

The following picture shows elements having more than 0.1% of the total strain energy of the 3rd mode.

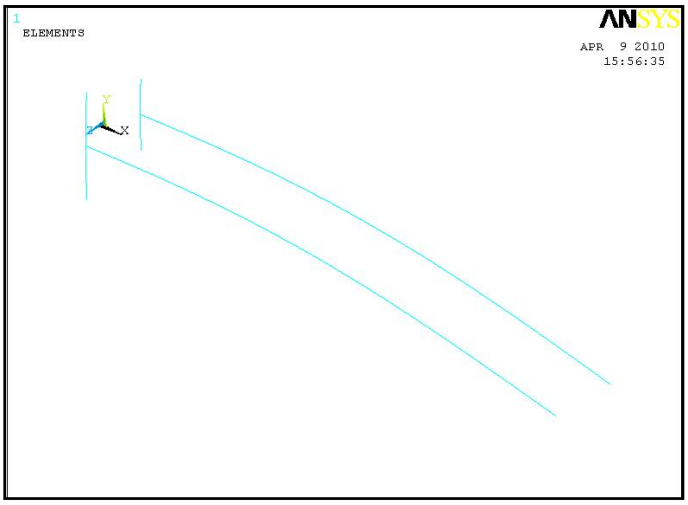

Figure 4.7 Elements with More than 0.1% of Total SE in 3rd Mode

Finally the picture below shows elements having more than 0.35% of the total strain energy of the 3rd mode.

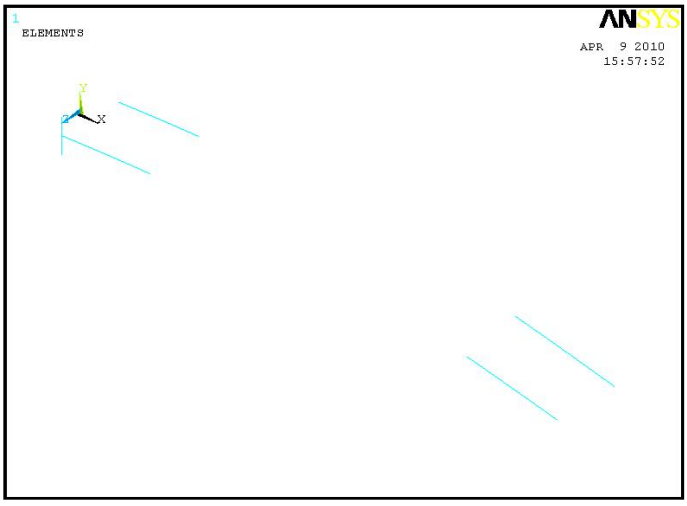

Figure 4.8 Elements with More than 0.35% of Total SE in 3rd Mode

5. HIGHLY ACCURATE SINGLE DOF EQUIVALENT MODEL OF COMPLEX SOLAR ARRAY

5.1 Motivation

The current model of the solar array has thousands of degrees of freedom, making the model very complex which consequently increases the processing time for different type of analyses. Since simple equivalent models are widely interested, as long as their results are within an acceptable range of accuracy; a study on finding a novel single degree of freedom equivalent model for the first translational and the first rotational modes of the solar array is conducted. These novel equivalent models can be used for parametric studies in different analyses. For instance, they are used in modal analysis to predict changes in natural frequency of the corresponding modes by any change in one of the system parameters, like tension load in Tension Wires.

5.2 Highly Accurate SDOF Equivalent Model for the First Mode

Based on the results obtained from modal analysis, the first mode of the solar array is a bending mode in the array.

A similar case with different boundary condition is assumed. Consider the array in the MCAs level and then set all DOFs at both ends to zero. Modal analysis results show the importance of role of tension loads in the dynamical behavior of bending modes. Based on the observations on the first mode shape, it was found that a simple

string model with equivalent mass can be used as an accurate equivalent model for the solar array bending mode shapes.

As can be found in many fundamentals of vibrations textbooks, natural frequencies of a simple string with fixed ends can be obtained from

$$f_n = \frac{n}{2L}\sqrt{\frac{T0}{\rho}} \quad \text{Hz}$$

where T0 denotes the tension load in the string and ρ is the mass of the unit length of the string [36]. ρ can be calculated as

$$\rho = \frac{m_{MCAs}}{L}$$

where L denotes the length of the array.

After substituting the numeric values, the n-th natural frequency, in Hz, for the equivalent model can be found as

$$f_n = 0.2616\, n$$

The following table shows the error between the natural frequency of the MCA model and the equivalent simple string model for the first 3 bending modes.

Table 5.1 MCA Model vs. Equivalent Simple String Model

Mode	% Error
1st bending mode	6.1
2nd bending mode	5.9
3rd bending mode	5.7

This shows that the equivalent simple string model works perfectly in predicting the natural frequencies and therefore can be used in parametric study of bending modes and parametric studies of the array.

5.3 Highly Accurate SDOF Equivalent Model for the Third Mode

Based on the results obtained from modal analysis, the third mode shape of the solar array is the first rotational mode.

Meirovitch develops a formula for the equation of motion of a vibrating pre-tensioned string assuming both potential and kinetic energies in [37]. By inspecting through the third mode shape and considering the fact that the frequency of this mode is much lower than the first natural frequency of a single MCA, it can be concluded that the kinetic energy in this mode is mainly due to the rotation of the MCAs and the restoring force is due to the tension load. Furthermore, in this mode, the Tension Wires make a sinusoidal wave where the amplitude of this wave at both ends of the array is zero. Therefore the equation describing the shape of the Tension Wires can be written as

$$y(x,t) = q(t)\sin\left(\frac{\pi x}{L}\right)$$

where $q(t)$ is the modal coordinate, x denotes the distance along the array measured from one end and L is the length of the array.

The following picture shows how the Tension Wires look like in the third mode as well as the way the above equation is defined for the shape of Tension Wires.

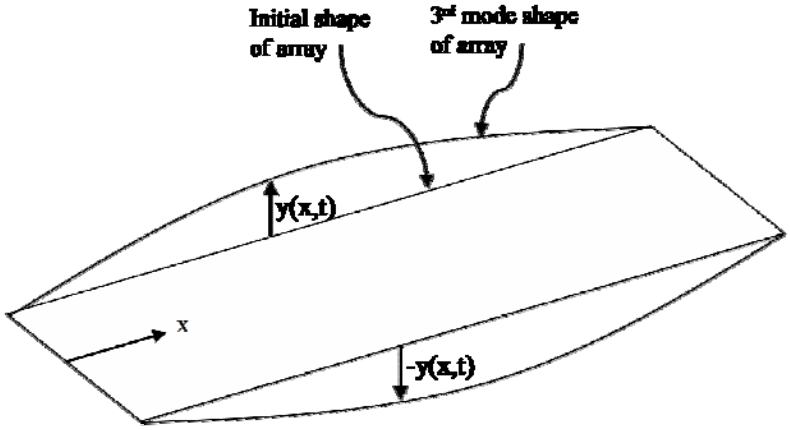

Figure 5.1 Definition of Physical Coordinate for the Equivalent Model

Potential energy for a single Tension Wire, in this mode, can be written as [37]

$$V_1(x) = \frac{1}{2}\int_0^L T(x)\left(\frac{\partial y(x,t)}{\partial x}\right)^2 dx$$

Assuming constant tension load we have

$$V_1(x) = \frac{1}{2}\int_0^L T0\left(\frac{q(t)\pi}{L}\right)^2 \cos^2\left(\frac{\pi x}{L}\right) dx = \frac{\pi^2\, T0}{4\, L}\, q(t)^2$$

Therefore the total potential energy would be

$$V(x) = 2\, V_1(x) = \frac{\pi^2\, T0}{2\, L}\, q(t)^2$$

As mentioned above, the kinetic energy term comes from the rotation of the MCAs. The angle of rotation for i-th MCA can be found from

$$\theta_i(x,t) = \frac{y_i(x,t)}{\frac{d}{2}} = \frac{2\, y_i(x,t)}{d}$$

where d denotes the width of the array.

Then the kinetic energy of the i-th MCA can be written as

$$T_i(t) = \frac{1}{2} I_p \dot{\theta}_i^{\,2} = \frac{2}{d^2} I_p \dot{q}(t)^2 \sin^2\left(\frac{\pi i}{N_{MCAs}}\right)$$

where N_{MCAs} is the total number of MCAs in the array, I_p is the mass moment of inertia of a single MCA about the array longitudinal axis.

Then using Lagrange equation of motion [38]

$$\frac{d}{dt}\left(\frac{\partial T}{\partial \dot{q}}\right) + \left(\frac{\partial V}{\partial q}\right) = 0$$

we have

$$\left(\frac{I_p}{d^2} \sum_{i=1}^{N_{MCAs}} \sin^2\left(\frac{\pi i}{N_{MCAs}}\right)\right) \ddot{q}(t) + \left(\frac{\pi^2 T0}{L}\right) q(t) = 0$$

From this equation the natural frequency, in Hz, for this mode can be found as

$$f = \frac{1}{2\pi} \sqrt{\left(\frac{\frac{\pi^2 T0}{L}}{\frac{I_p}{d^2} \sum_{i=1}^{N_{MCAs}} \sin^2\left(\frac{\pi i}{N_{MCAs}}\right)}\right)}$$

In order to check the robustness of the derived equivalent model with respect to the parameter T0, the modal analysis is performed for different T0 values and the results are compared to what that can be predicted using the equivalent model. The following graph shows the frequency prediction of the equivalent model and the actual frequency obtained from performing modal analysis on the solar array with respect to changes in tension load. The values are removed due to proprietary restrictions.

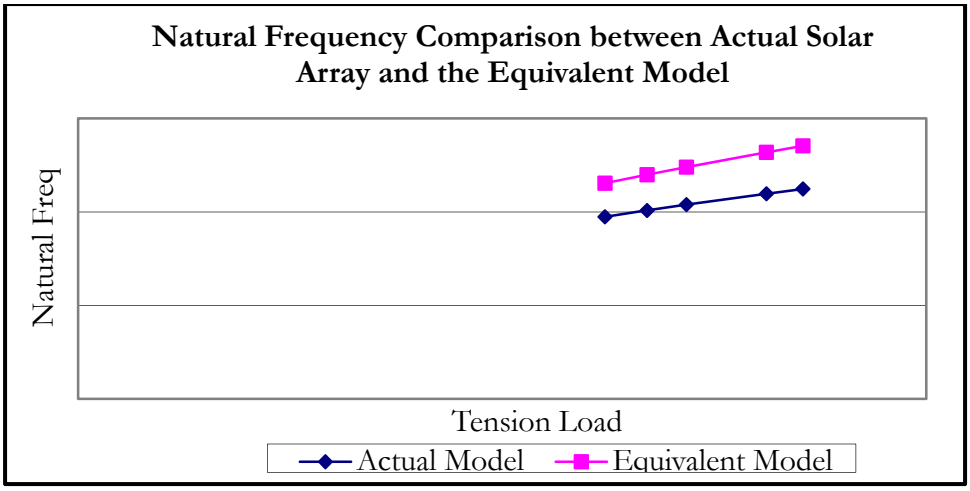

Figure 5.2 Natural Frequency Comparison between Actual Solar Array and the Equivalent Model

Based on the results obtained from the parametric study, the equivalent model is capable of predicting the natural frequency of the 3rd mode of the solar array, within 20% of accuracy, by changing the tension load. It is an interesting result since the equivalent model has single DOF while the actual model has thousands of DOF and hence obtaining the natural frequency for different tension loads requires a new running of the whole model and would be time-consuming.

6. FULL NONLINEAR TRANSIENT ANALYSIS AND POINTING ERROR

6.1 Introduction

Transient analysis is the study of the dynamic response of a structure under the action of any general time-dependent loads. It can be used to determine the time-varying displacements, strains, stresses and forces in a structure as it responds to any combination of static, transient and harmonic loads. The results obtained from this analysis can be used to assess changes in a physical quantity at a specific place within the structure with respect to time or the value of that quantity at a specific time over the entire structure.

Since satellites experience many different maneuvers most of the time, performing transient analysis under different types of loadings is an essential step in satellite design. This section presents full nonlinear transient analysis study on the solar array under Solar Wing Drive (SWD) maneuver in GEO and LEO orbits. Array-level pointing error which is a measure of the accuracy of the Sun tracking maneuver that is related to energy generating performance of the solar array will be introduced as one of the important postprocessing analyses performed on the transient analysis results and the corresponding results will be provided in detail later in this section. The concentrator array will have higher pointing requirements than a traditional array.

The y-axes values in this section are eliminated due to proprietary restrictions on Boeing and DR Technologies data.

6.2 Array-Level Pointing Error

Array-level pointing error refers to the error between the coordinates that the solar array has practically occupied during a specific maneuver and the coordinates that it was supposed to be at, assuming rigid-body array. Many factors influence this error such as the relative motion between MCAs. A smaller pointing error indicates that the Sun tracking maneuver is accomplished with high accuracy resulting in higher energy generating performance. Based on the solar array design objectives and requirements, a budget for the pointing error will be defined. This means that a good performance in the Sun tracking maneuver can be achieved if the time history plot of the total pointing error does not exceed the budget value.

Here, the pointing error caused by the relative motion between MCAs is considered. Other type of pointing errors should be studied separately and compared individually to their corresponding budget values.

After inspecting all possible scenarios that might happen during array maneuvers, 3 sources of relative motions between MCAs that contribute to this type of pointing error are identified. The total pointing error, or error sum, would be the algebraic summation of all individual errors. They are summarized as follows:

- Error 1: Relative X motion causes image to go out-of-focus.
- Error 2: Relative Y motion causes focal line to move.
- Error 3: Relative Theta-Z motion causes focal line to move.

Since relative motion between MCAs is being considered, each MCA needs to have a local coordinate system attached rigidly to it so that the relative motions can be viewed from these coordinate systems. These coordinate systems are called MCAs Local Frames and shown in the following picture.

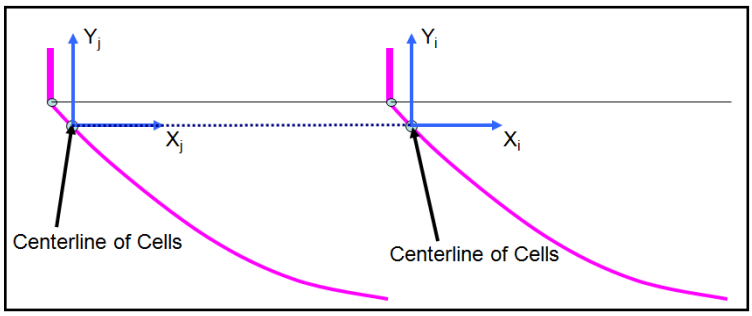

Figure 6.1 MCAs Local Frames

6.2.1 Error 1

As shown below, this error is due to the relative motion of MCAs in the X-direction and causes the image to spread.

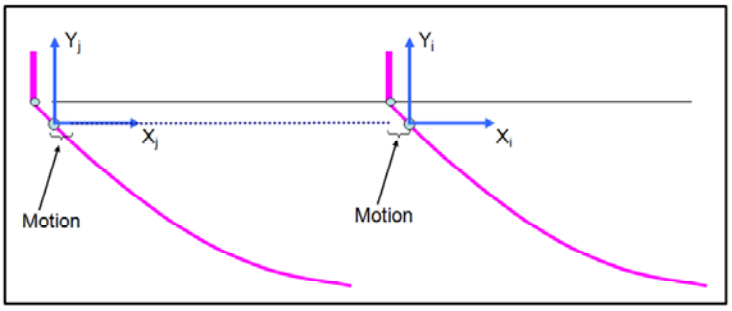

Figure 6.2 Definition of Pointing Error 1

6.2.2 Error 2

This error is due to the relative motion of MCAs in Y-direction and causes the focal line to move. It is shown graphically in the following picture.

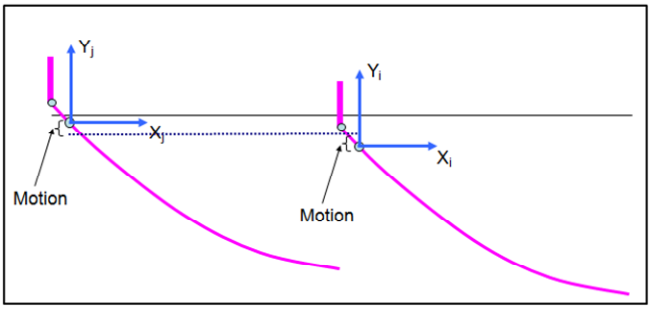

Figure 6.3 Definition of Pointing Error 2

6.2.3 Error 3

This error, shown below, is due to the Z-rotation of MCAs and causes the focal line to move.

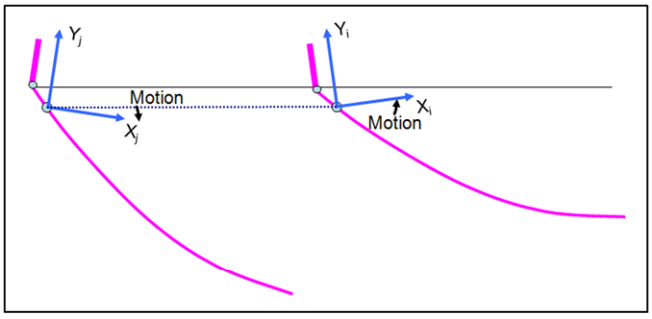

Figure 6.4 Definition of Pointing Error 3

6.3 Transient Analysis under Solar Wing Drive (SWD) in GEO Orbit

6.3.1 SWD Input in GEO Orbit

Solar Wing Drive (SWD) is a maneuver of the solar array to track the Sun. The objective is to keep the orientation of solar array in a direction that the array receives maximum sunlight all the time as the Earth moves around itself. SWD is applied as a rotational input about the longitudinal axis of the array passes through the center of gravity.

From the motor specifications and required maneuver objectives, the period of the input profile is calculated as 9.6 second.

Frequency of the input profile for SWD in the GEO orbit can be calculated as

$$f_{SWD,GEO} = \frac{1}{T_{SWD,GEO}} = 0.104\ Hz$$

6.3.2 Steps to Obtain Flexible Displacements in Local Rotating Frame

Pointing error calculations are based on the MCAs Local Frames attached to MCAs, therefore the rigid motion of MCAs should be taken out from the total displacements to obtain flexible displacements.

In SWD maneuver, in addition to the MCAs Local Frames which are rigidly attached to the MCAs, two major coordinate systems are defined:

- **Global Frame** which is fixed in the space.
- **Local Rotating Frame** with its origin at the origin of the global frame and capable of rotating.

To examine the difference between the results viewed in the global and local rotating frames, the time history of the displacement a specific node under SWD input in the GEO orbit is considered and plotted as viewed from these two coordinate systems.

The steps to obtain the flexible displacements sensed in the local rotating frame are summarized below.

- *Step 1: Finding rigid location of nodes in the global frame*

The following picture shows the rigid coordinate of the considered node in the global frame.

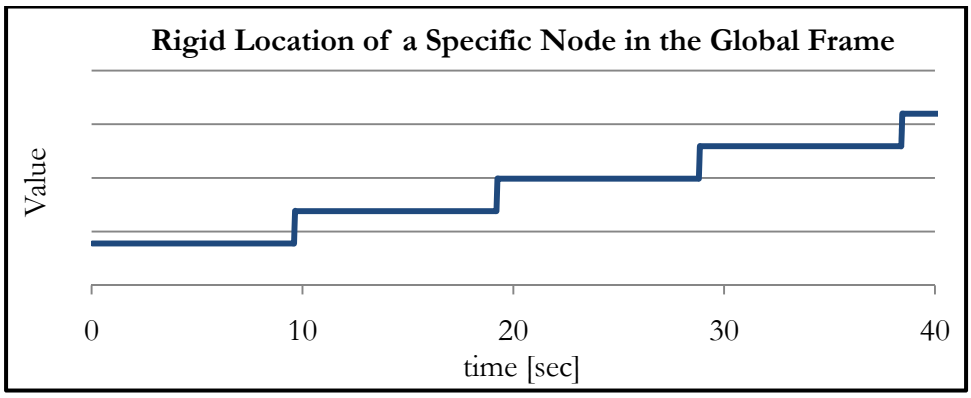

Figure 6.5 Rigid Location of a Specific Node

- *Step 2: Finding total (rigid + flexible) location of the nodes in the global frame*

This can be obtained from ANSYS output result file. The following picture shows the total location of the node considered in the global frame.

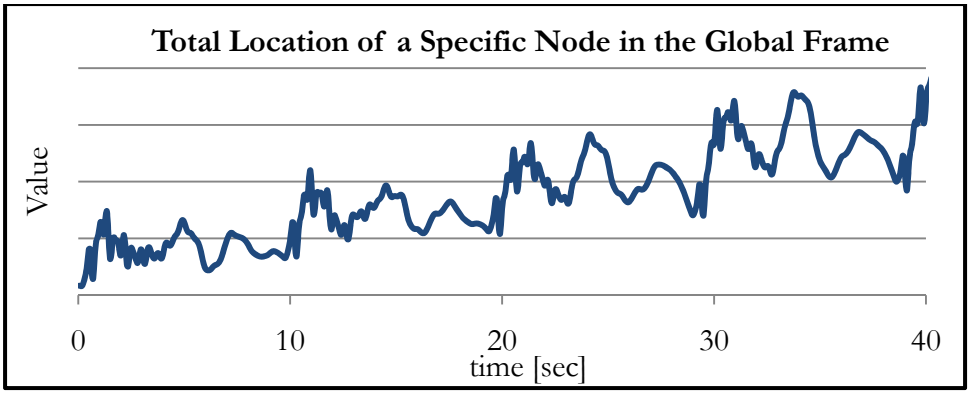

Figure 6.6 Total Location of a Specific Node

- *Step 3: Finding flexible displacements in the global frame*

By subtracting the rigid location from the total location, both sensed in the global frame, at each sub step for each node, the flexible displacement can be obtained. The following pictures shows the flexible displacement sensed in the global frame for that specific node.

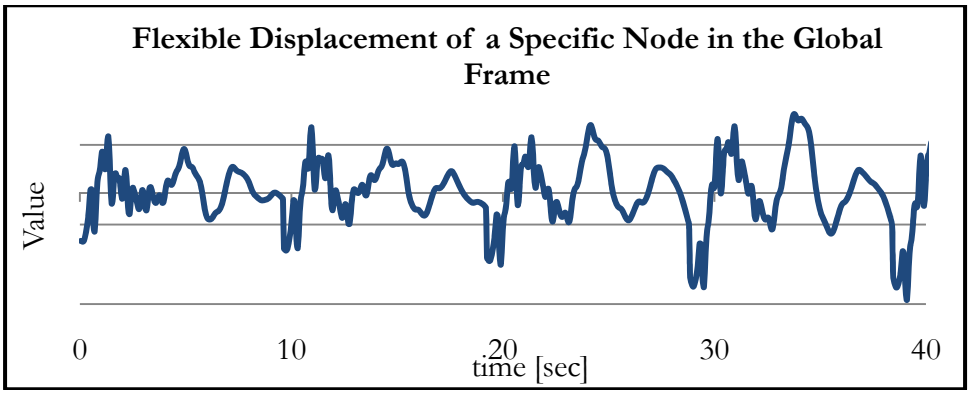

Figure 6.7 Flexible Displacement of a Specific Node in the Global Frame

- *Step 4: Coordinate Transformation*

Having the displacements in the global frame and using coordinate transformation, the flexible displacements in the local rotating frame can be obtained. The following picture is showing the flexible displacements of that specific node as sensed in the local rotating frame.

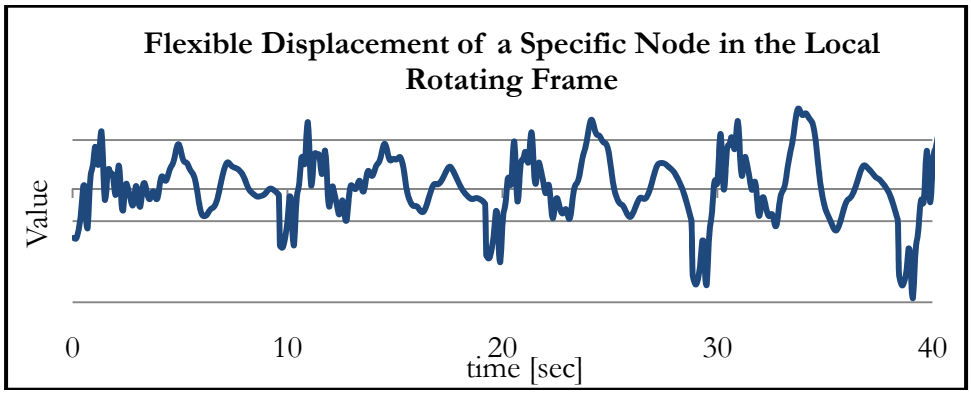

Figure 6.8 Flexible Displacement of a Specific Node in the Local Rotating Frame

The last two plots are not exactly identical, but the difference might not be enough clear because the total angle of rotation was very small.

6.3.3 Transient Displacement Response under SWD GEO

In most transient analyses transient displacement plots are one the objectives because many information regarding the dynamical behavior of the structure can be extracted from displacement plots; like the required time to reach steady state response, maximum displacement at transient state and at steady state, identifying dominant higher and/or lower natural frequencies participating in the response by performing Fast Fourier

Transform study, etc. As an example, the following graph shows the transient displacement plot of a specific node under SWD GEO input.

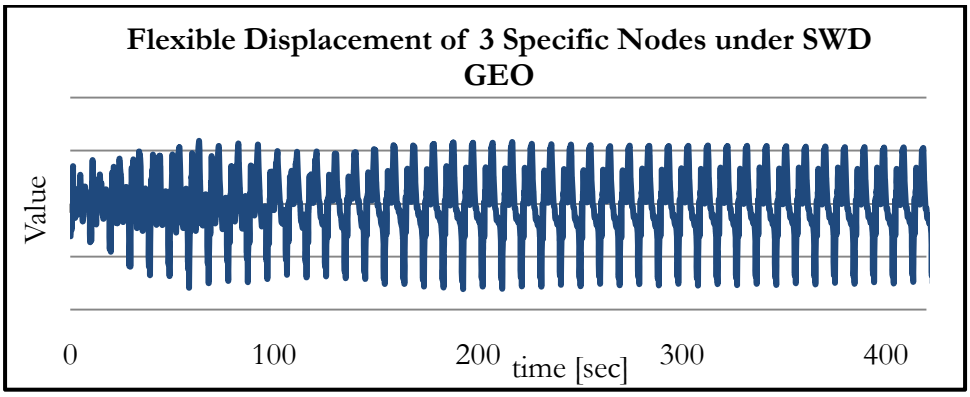

Figure 6.9 Flexible Displacement of a Specific Node under SWD GEO

The following plot shows the steady state portion of the response shown above for that specific node.

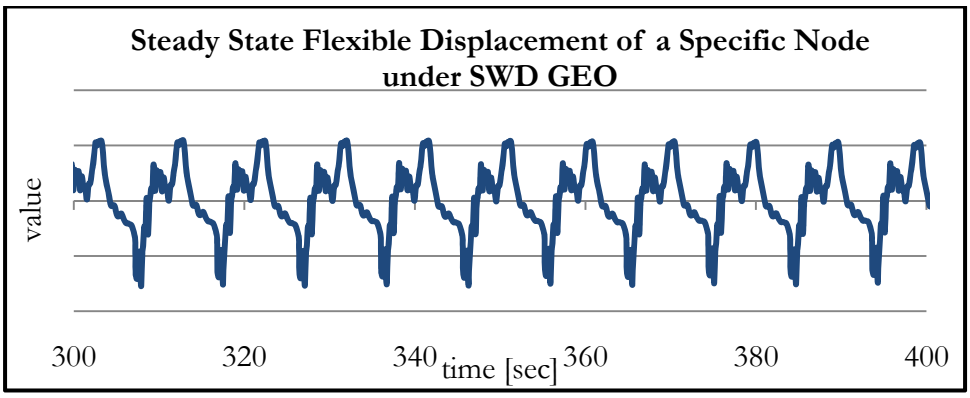

Figure 6.10 Steady State Flexible Displacement of a Specific Node under SWD GEO

6.3.4 Fast Fourier Transform Study on Transient Response under SWD GEO

In the frequency domain, vibration analysis may be carried out using Fourier transform techniques. In 1965 the Fast Fourier Transform (FFT) algorithm was published by Cooley and Tukey [31], [39], [40].

Fast Fourier Transform is a powerful tool in obtaining the natural frequency spectrum of the response, transient and/or steady state, of a structure under a loading condition [31]. In the frequency spectrum obtained from Fast Fourier Transform of a transient response, frequencies having higher amplitudes have mode shapes greatly participate in the response of the structure compared to other mode shapes.

A Fast Fourier Transform study is performed on the steady state portion of displacement response under SWD GEO input obtained. The following graph shows the steady state portion of the displacement response considered for the FFT study.

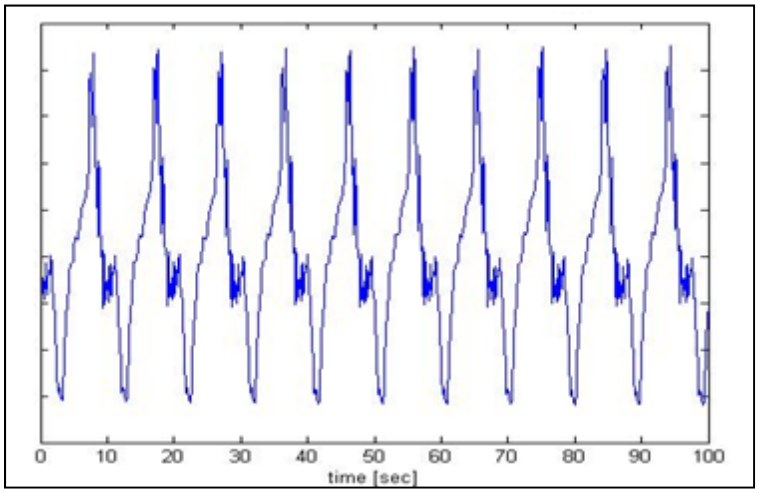

Figure 6.11 Steady State Transient Response of a Specific Node under SWD GEO

The following graph shows the frequency spectrum obtained after performing FFT analysis on the above transient response graph.

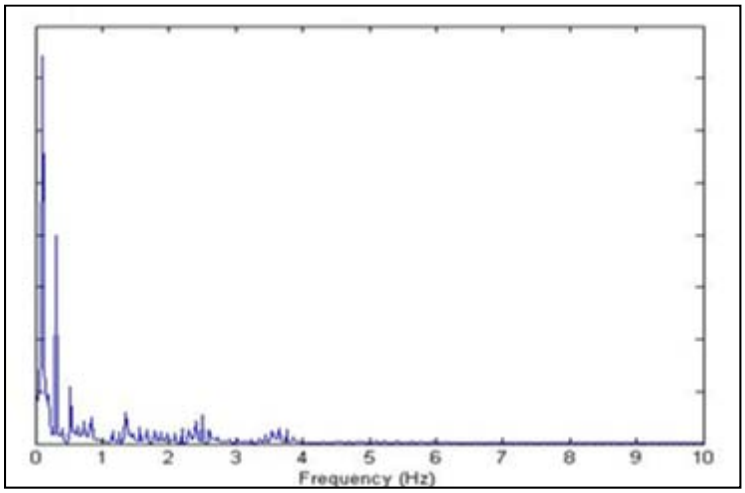

Figure 6.12 Frequency Spectrum for the Transient Response of a Specific Node under SWD GEO

The first highest peak of the above frequency spectrum graph is near one of the natural frequencies of the array. Therefore the current design for SWD input in GEO orbit excites one of array modes. The following pictures show a number of modes may participate in the transient response under current SWD GEO input.

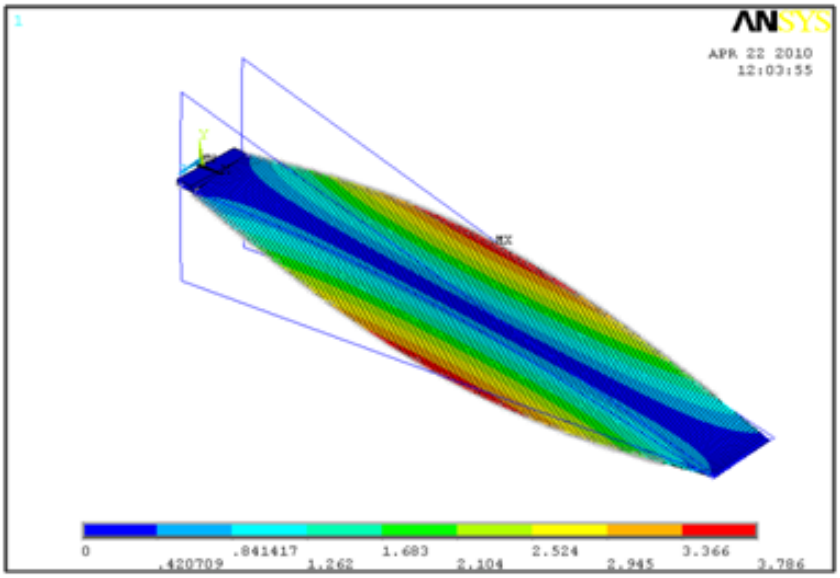

Figure 6.13 One of the Array Mode Shape Participating with a Large Factor in the Transient Response

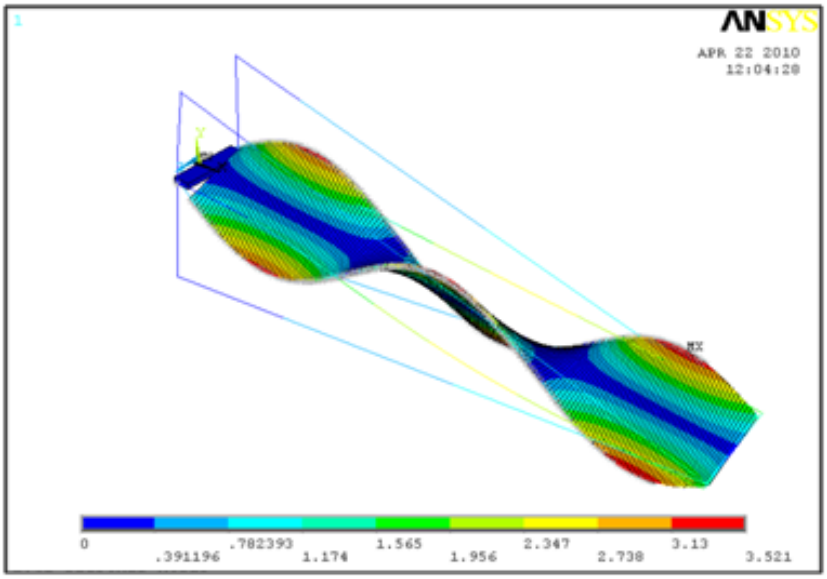

Figure 6.14 One of the Array Mode Shapes Participating with a Relatively Considerable Factor in the Transient Response

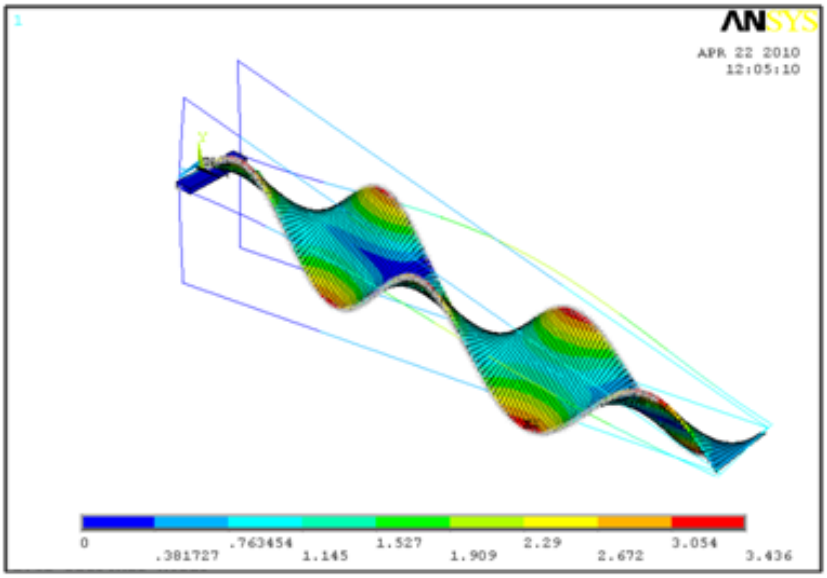

Figure 6.15 One of the Array Mode Shapes Participating with a Small Factor in the Transient Response

Theses mode shapes participate in the transient response with different order of magnitudes depending on their modal effective mass. Those having larger modal effective mass participate more and become the dominant component in the transient response.

6.4 Pointing Error Calculations for the Solar Array under SWD GEO

Pointing error calculation is an important result of the transient analysis which is useful for energy generating performance considerations. After calculating the pointing error using transient response the following graphs are obtained for the error sum of two specified MCAs.

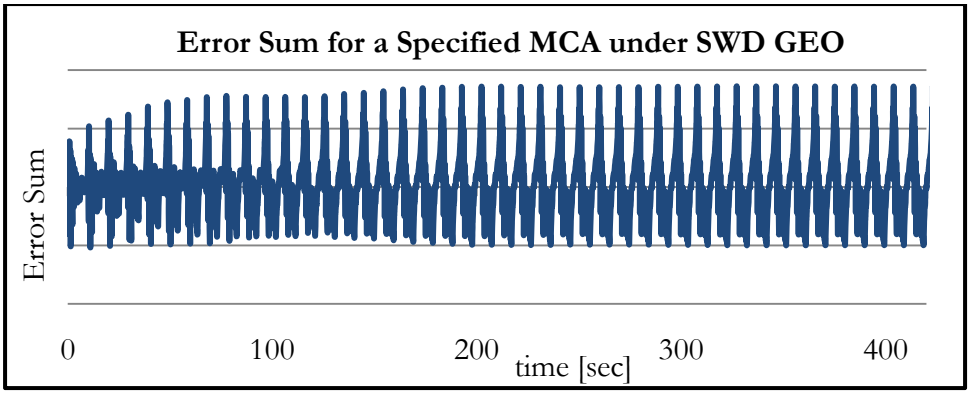

Figure 6.16 Error Sum for a Specified MCA under SWD GEO

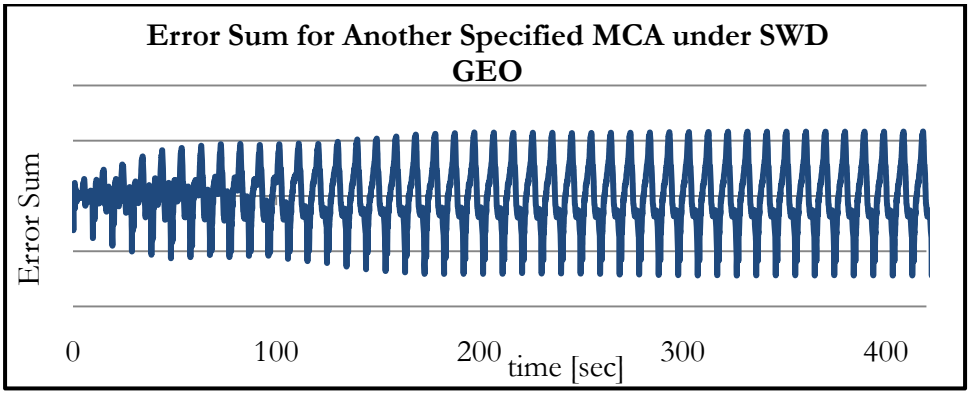

Figure 6.17 Error Sum for another Specified MCA under SWD GEO

It is important to find the maximum instantaneous error sum over all MCAs to identify the MCAs having maximum error sum at each time and also check whether this maximum value exceeds the budget or not. The maximum instantaneous error sum over all MCAs under SWD input in GEO orbit is plotted in the following graph.

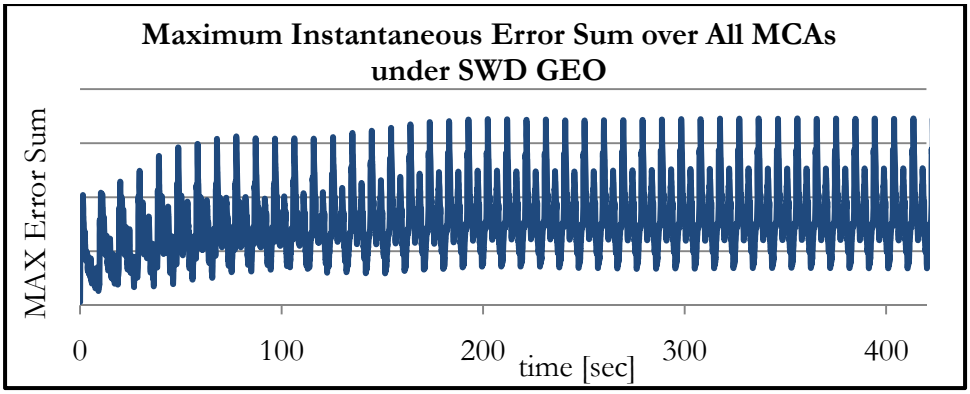

Figure 6.18 Maximum Instantaneous Error Sum over All MCAs under SWD GEO

This graph shows that the maximum instantaneous error sum over all MCAs under SWD GEO is a bounded value. It does not exceed the budget value, therefore the current design meets the requirements. This indicates that Sun tracking under SWD in GEO orbit can be efficiently performed in sense of energy generating performance.

6.5 Improving Pointing Error by Exploring Different Staggering Type Inputs for the SWD GEO

6.5.1 Motivation

Exploring other possible options for SWD GEO input may be helpful in:

- Decreasing the maximum instantaneous pointing error
- Decreasing the amplitude of vibrations
- Decreasing the number of excited modes
- Decreasing the participation of critical modes

Two different staggering type inputs for SWD in GEO orbit are proposed for further investigation on transient analysis response, Fast Fourier Transform (FFT) study

and pointing error calculations. Finally, the obtained results will be compared to those of current SWD GEO to determine the efficacy of the proposed inputs.

6.5.2 Current and Proposed SWD GEO Inputs

- *Case I: 9.6-9.6-Periods Input (Current Input)*

  This input has a single period of 9.6 seconds.

- *Case II: 14.4-4.8-Periods Input (Proposed)*

  One of the proposed solutions to this problem is to use an input signal having successive periods of 14.4 and 4.8 seconds, known as 14.4-4.8-periods input.

- *Case III: 4.8-4.8-Periods Input (Proposed)*

  One other option is to break down the current 9.6-second period into to two equal periods and apply half of the input amplitude in each period.

For each case of study, the transient responses of the same nodes will be compared. Then an FFT analysis is performed to identify the dominant participating modes in the transient response of each case. At last for each case, the pointing error will be calculated to determine the efficacy of the proposed inputs in the sense of improving the energy generating performance.

6.5.3 Comparison of the Transient Displacement Responses

One of the objectives of proposing new inputs for SWD GEO is to reduce the vibrations amplitude. Smaller amplitude of vibrations leads to better Sun tracking and therefore smaller pointing error. To compare the transient displacement responses under

these 3 inputs, the time history of displacement of a specific node is considered and plotted below for all cases.

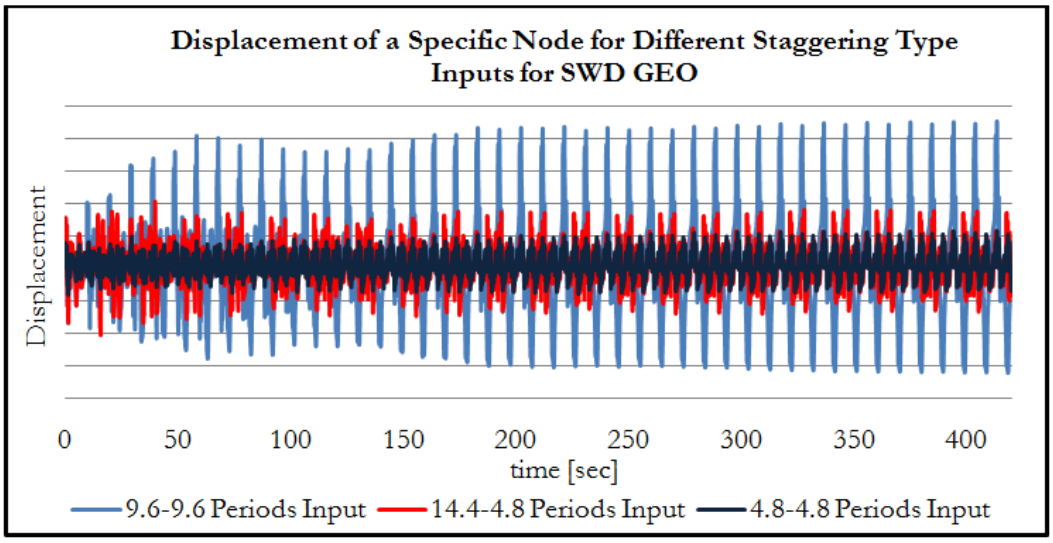

Figure 6.19 Transient Response under Different Inputs for SWD GEO

The proposed 14.4-4.8 and 4.8-4.8 inputs decreased the amplitudes of vibrations by 61% and 74% respectively. This proves the efficacy of the proposed inputs in reducing the pointing error as well as the amplitude of vibrations.

6.5.4 Comparison of the Fast Fourier Transform Results

FFT study is performed on the steady state portion of the transient responses shown above for all case to determine the participating frequencies and their level of importance. The following graphs show the steady state displacement responses considered for FFT study as well as the corresponding FFT results obtained. Scale of the transient response graphs are the same.

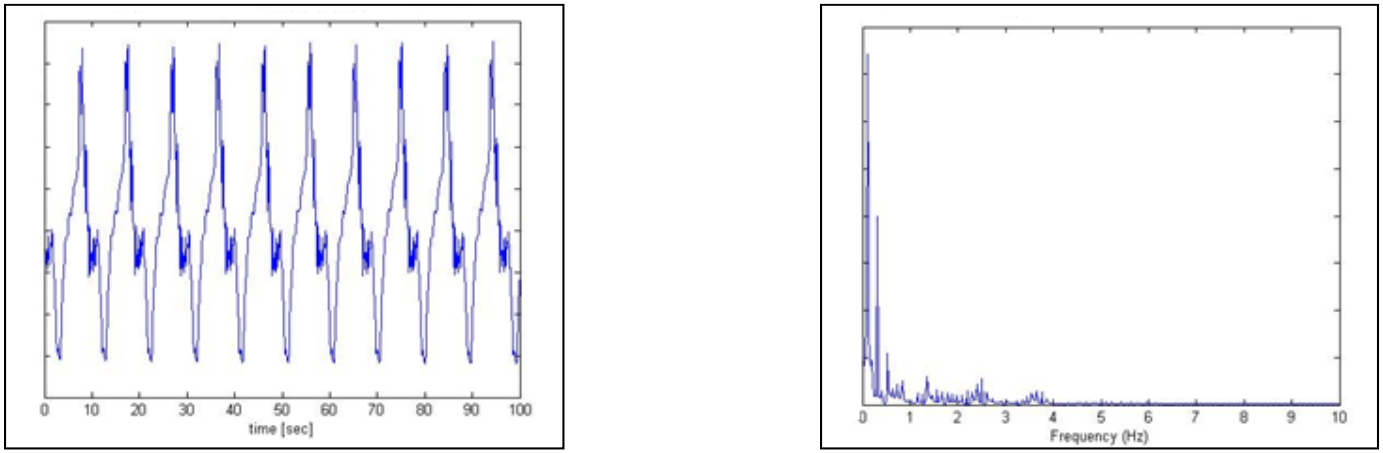

Figure 6.20 Transient Response (Left) and FFT (Right) Graphs for 9.6-9.6-periods Input for SWD GEO

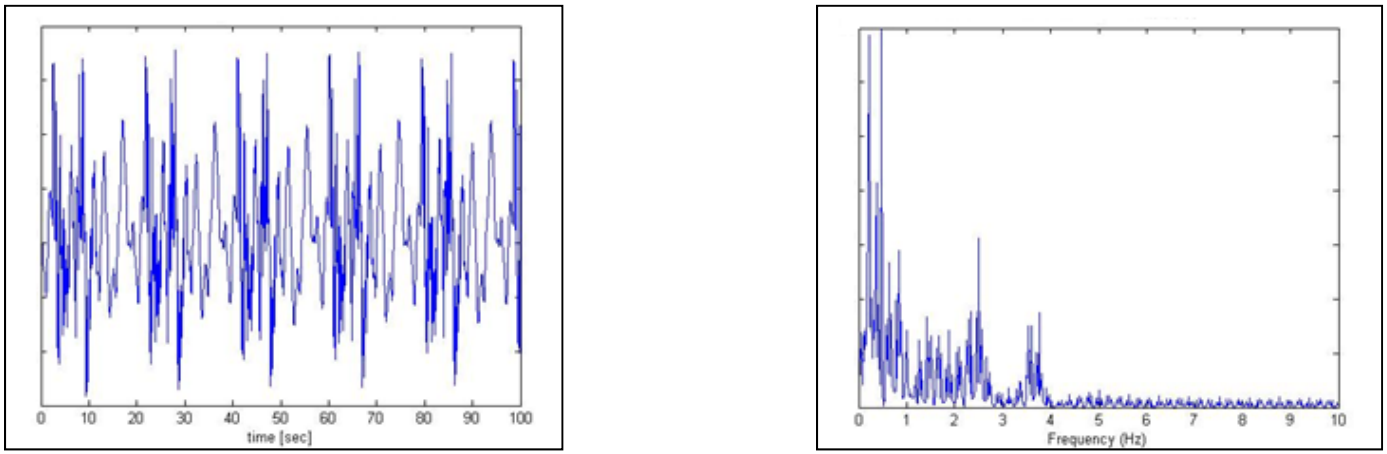

Figure 6.21 Transient Response (Left) and FFT (Right) Graphs for 14.4-4.8-periods Input for SWD GEO

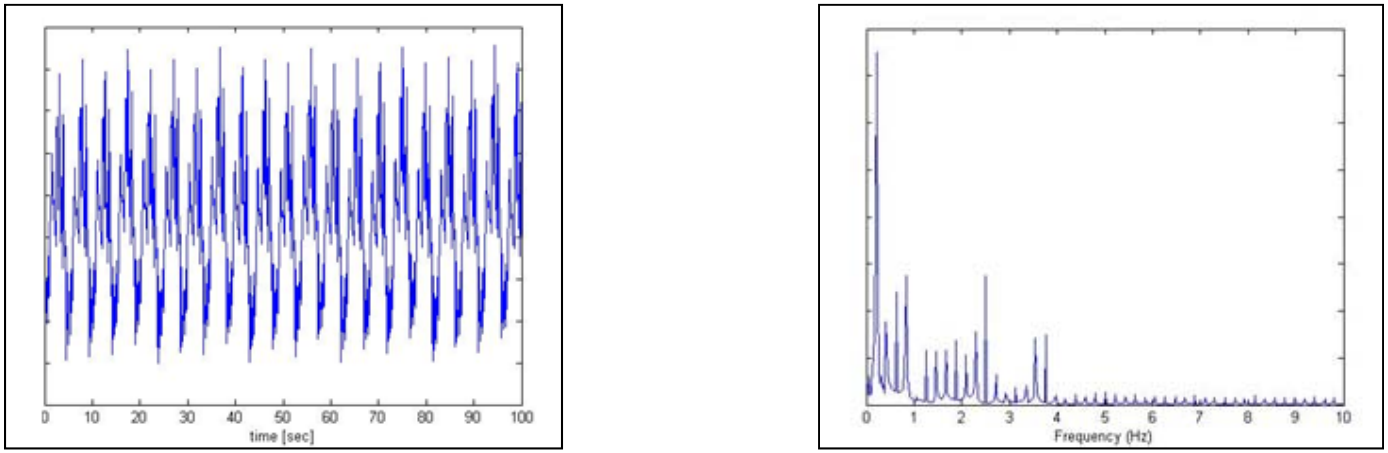

Figure 6.22 Transient Response (Left) and FFT (Right) Graphs for 4.8-4.8-periods Input for SWD GEO

Summary of the FFT results for all SWD GEO input cases are provided in the following table showing the significant natural frequencies participating in the transient response.

Table 6.1 Summary of FFT Results for All SWD GEO Input Cases

Scenario	MAX Absolute Displacement Reduction	Frequency [Hz] of the Major Excited Modes (FFT Result)						
		1st	2nd	3rd	4th	5th	6th	7th
9.6-9.6 Period	---	0.098	0.313	0.528	Not Significant			
14.4-4.8 Period	61% Reduction	0.470	0.215	0.372	2.505	0.842	0.626	Not Sig.
4.8-4.8 Period	74% Reduction	0.215	2.505	0.842	0.626	0.411	3.757	2.290

6.5.5 Comparison of the Pointing Errors

The main purpose of proposing new inputs for SWD GEO is to improve the pointing error. After performing postprocessing steps to calculate pointing error, the following plot for the maximum instantaneous error sum for the 3 cases of study obtained.

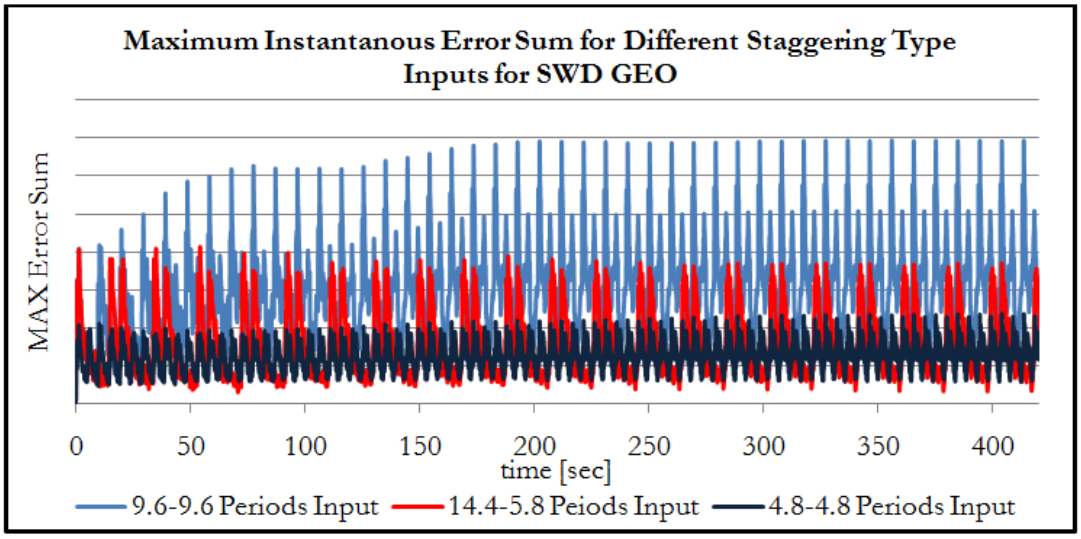

Figure 6.23 Maximum Instantaneous Error Sum under Different SWD GEO Inputs

This plot indicates an excellent achievement in improving the pointing error with the proposed 14.4-4.8-period and 4.8-4.8-period inputs by respectively 40% and 66% reduction in the current pointing error under 9.6-9.6-period input. This considerable reduction in the pointing error contributes to a higher energy generating performance of the solar array.

6.6 Transient Analysis under Solar Wing Drive (SWD) in LEO Orbit

6.6.1 SWD Input in LEO Orbit

From the specifications and design requirements of the input profile for SWD in LEO orbit, the period of this input is calculated as 0.4 seconds.

This results in a frequency of 2.5 Hz for the SWD input profile in the LEO orbit. At this frequency there is no large modal effective mass.

6.6.2 Transient Displacement Response under SWD LEO

As in the case of GEO orbit, the transient displacement plots show the time required for the vibrations to reach steady state as well as the maximum displacement in steady state. Transient plots can also be used for FFT study to identify the participating modes. The following plot shows the transient response of a specific node in the local rotating frame under SWD input in LEO orbit.

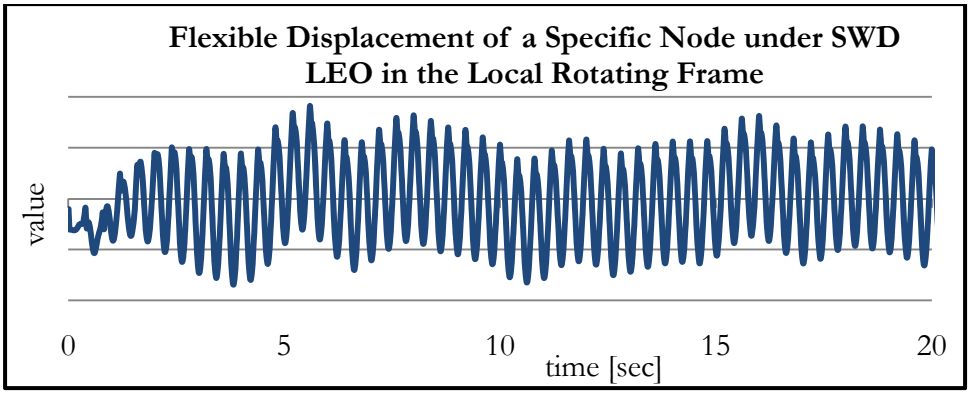

Figure 6.24 Transient Response of a Specific Node under SWD LEO in the LRF

The following graph shows the steady-state portion of the displacement response.

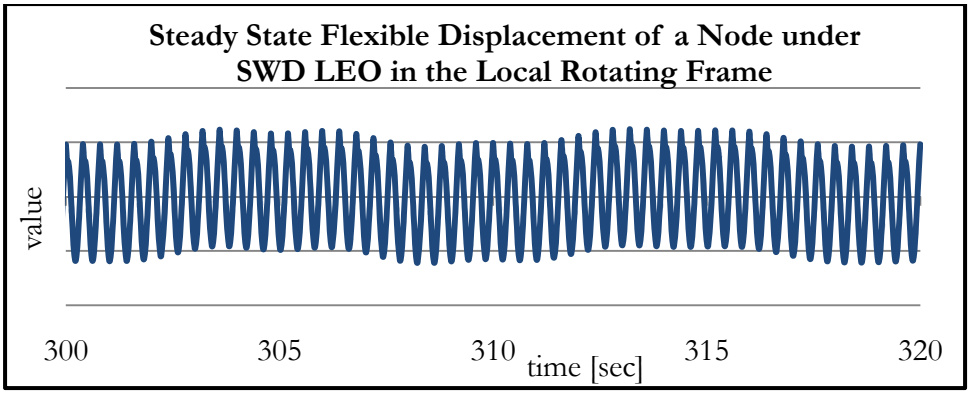

Figure 6.25 Steady State Flexible Displacement of a Specific Node under SWD GEO in the LRF

6.6.3 Fast Fourier Transform Study on Transient Response under SWD LEO

Fast Fourier Transform study is performed on the steady state portion of displacement response obtained above for that specific node. The following graph shows the steady state portion of the displacement response considered for the Fast Fourier Transform study.

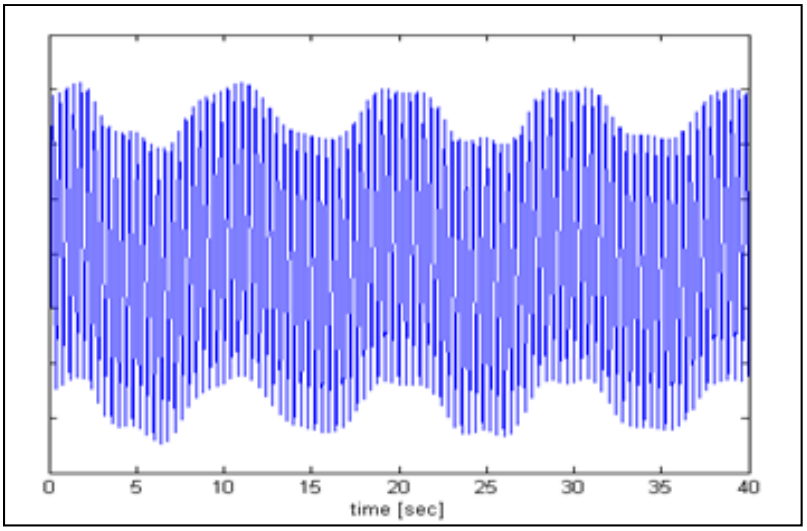

Figure 6.26 Steady State Flexible Displacement of a Specific Node under SWD LEO for FFT Study

The following graph shows the frequency spectrum obtained from performing Fast Fourier Transform analysis on the above graph. As can be seen there are two main frequencies participating in the transient displacement response under SWD LEO. The highest peak in the frequency spectrum plot corresponds to the frequency of 2.5 Hz which is the frequency of SWD LEO input. Referring to the modal analysis results, at this frequency there is no considerable modal effective mass and therefore it does not have any serious consequence. The second highest peak occurs at the frequency of 0.098 Hz which is very close to the first rotational mode natural frequency, 0.104 Hz; but the amplitude of graph at this frequency is less than 30% of the first major one amplitude at 2.5 Hz.

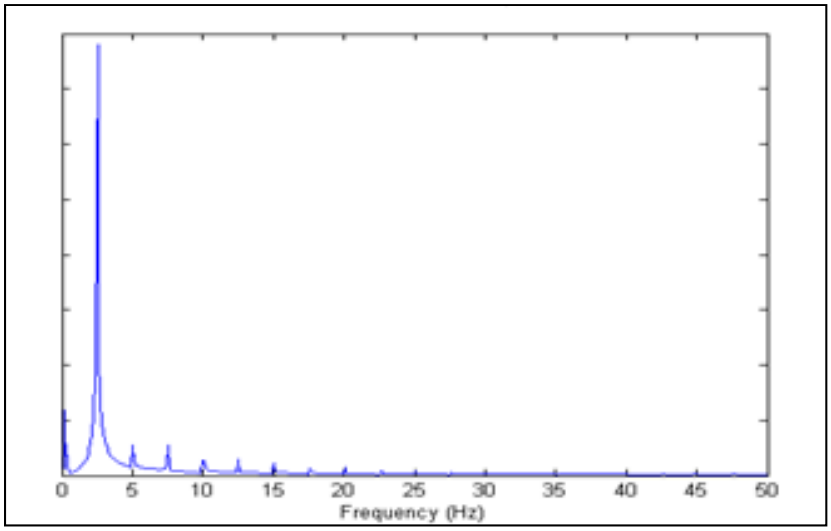

Figure 6.27 Frequency Spectrum Plot for the Flexible Displacement of a Specific Node under SWD GEO

6.7 Pointing Error Calculations for the Solar Array under SWD LEO

Following the same postprocessing steps to calculate the pointing error; the maximum instantaneous error sum over all MCAs under SWD LEO input obtained as shown below. Having more successive impulses in certain amount of time for LEO orbit compared to the GEO orbit, prevents the vibrations to damped enough before applying the next impulse which results in higher pointing error. This can be seen in the graph shown above for the LEO orbit.

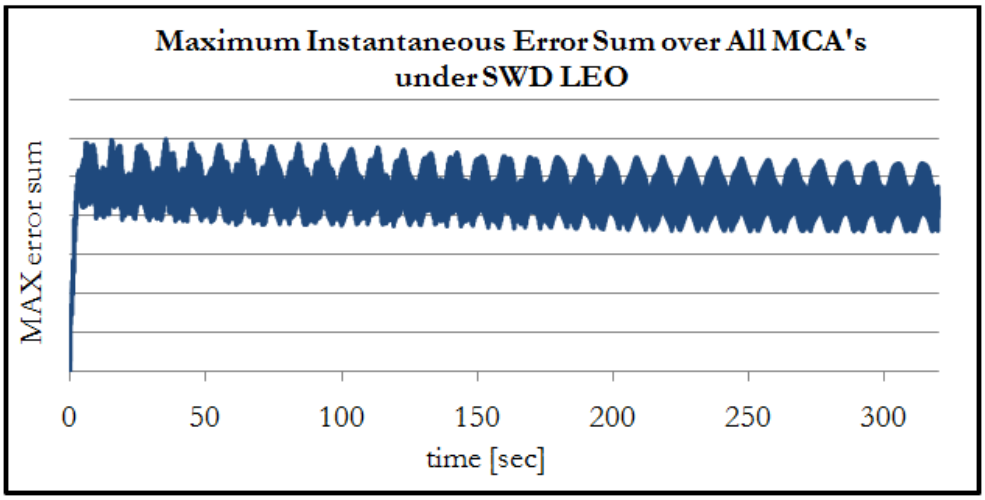

Figure 6.28 Maximum Instantaneous Error Sum over All MCAs under SWD LEO

6.8 Improving Pointing Error by Exploring Different Staggering Type Inputs for the SWD LEO

6.8.1 Motivation

Exploring other input options may help to reduce the pointing error and have a better performance. Therefore 2 different staggering type inputs are proposed and pointing error study is conducted to determine the efficacy of the new inputs.

6.8.2 Current and Proposed SWD LEO Inputs

- *Case I: 0.4-0.4-Periods Input (Current Input)*

  This input has a single period of 0.4 seconds.

- *Case II: 0.6-0.2-Periods Input (Proposed)*

  One proposed input is to use successive 0.6-second and 0.2-second periods and apply the same input amplitude in each interval.

- *Case III: 0.2-0.2-Periods Input (Proposed)*

Another idea is to break down the current input's period into two equal intervals and apply half of the input amplitude in each interval. This will results in an input with a frequency of twice the current design.

For each case of study, the transient responses of the same nodes will be compared. Then an FFT analysis is performed to identify the dominant participating modes in the transient response of each case. At last for each case, the pointing error will be calculated to determine the efficacy of the proposed inputs in the sense of improving the energy generating performance.

6.8.3 Comparison of the Transient Displacement Responses

To compare the transient displacement responses under these 3 inputs, the time history of displacement of a specific node in local rotating frame is considered and plotted below for all cases.

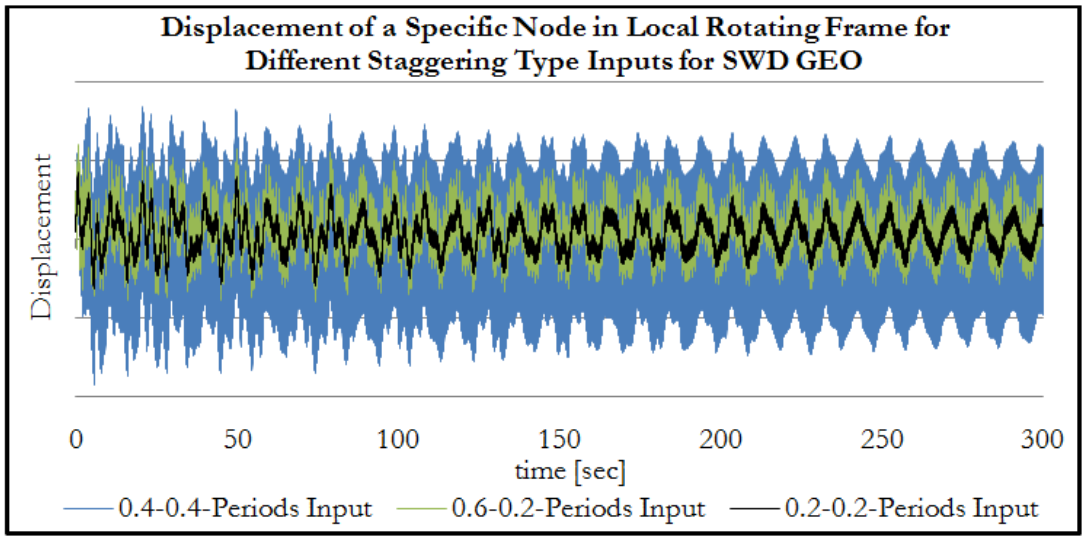

Figure 6.29 Transient Response under Different Inputs for SWD LEO

Using proposed 0.6-0.2-period and 0.2-0.2-period SWD LEO inputs decreases the amplitude of vibrations in the steady state region by 30% and 62% respectively which indicates the efficacy of the proposed inputs for SWD LEO and leads to smaller pointing error and consequently a better Sun tracking.

6.8.4 Comparison of the Fast Fourier Transform Results

The following graphs show the steady state flexible displacement responses considered for the Fast Fourier Transform study as well as the frequency spectrum plot obtained for the 3 cases of study. Scale of the transient response graphs are the same.

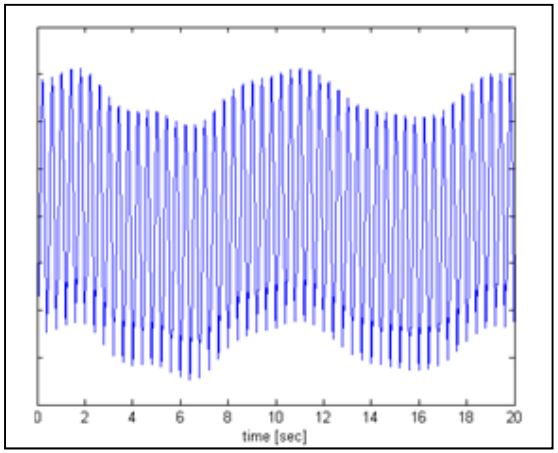

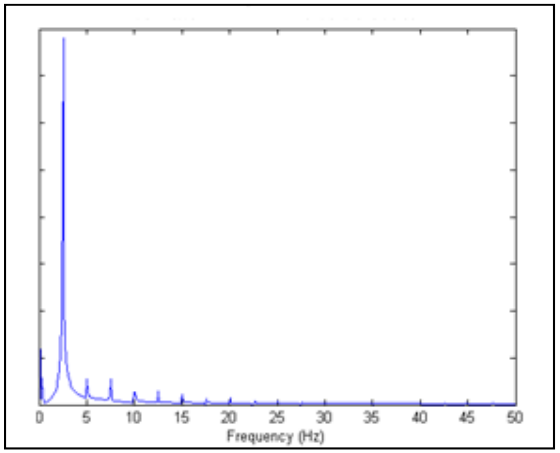

Figure 6.30 Transient Response (Left) and FFT (Right) Graphs for 0.4-0.4-periods Input for SWD LEO

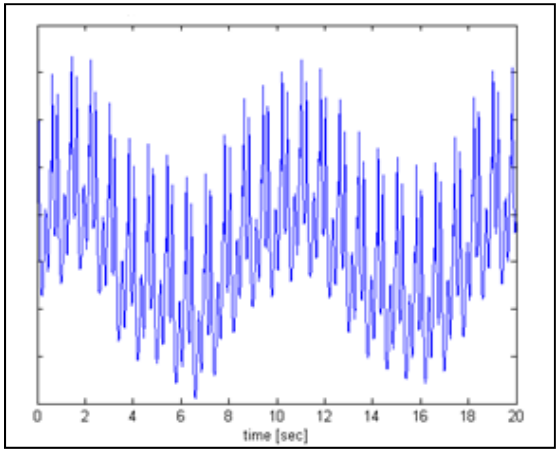

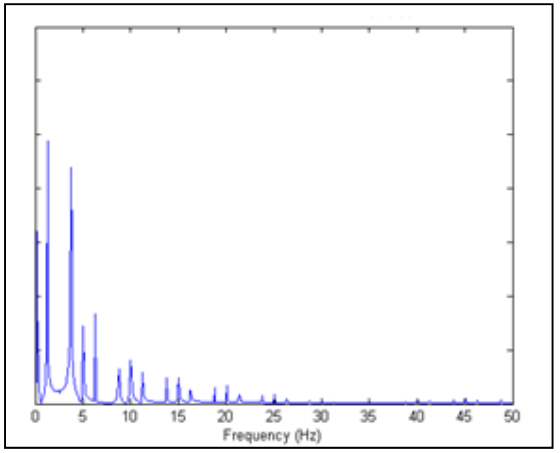

Figure 6.31 Transient Response (Left) and FFT (Right) Graphs for 0.6-0.2-periods Input for SWD LEO

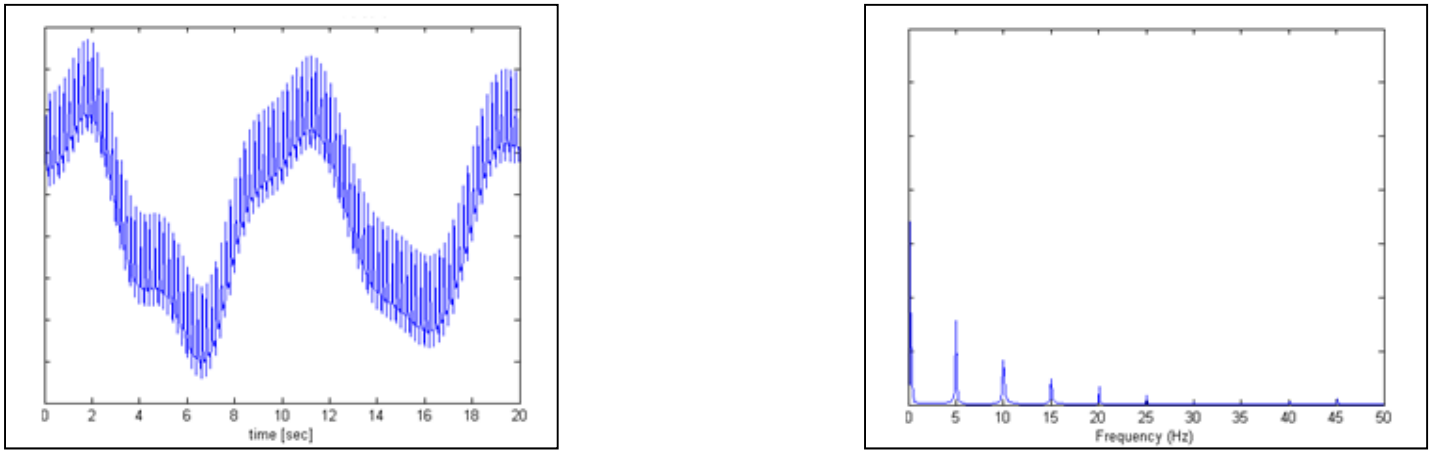

Figure 6.32 Transient Response (Left) and FFT (Right) Graphs for 0.2-0.2-periods Input for SWD LEO

Summary of the Fast Fourier Transform results for all SWD LEO input cases are provided in the following table showing the significant natural frequencies participating in the transient response.

Table 6.2 Summary of FFT Results for All SWD GEO Input Cases

Scenario	MAX Absolute Displacement Reduction	Frequency [Hz] of the Major Excited Modes (FFT Result)				
		1st	2nd	3rd	4th	5th
0.4-0.4 Period	---	2.544	0.098	0.528	Not Significant	
0.6-0.2 Period	31% Reduction	0.098	1.272	3.718	6.262	4.990
0.2-0.2 Period	63% Reduction	0.098	0.294	4.990	9.980	Not Sig.

6.8.5 Comparison of the Pointing Errors

Since the main motivation for proposing new inputs for SWD LEO is to decrease pointing errors, the pointing error calculation results will have a priority in optimal design considerations. The following graph summarizes these calculations for the 3 cases of study.

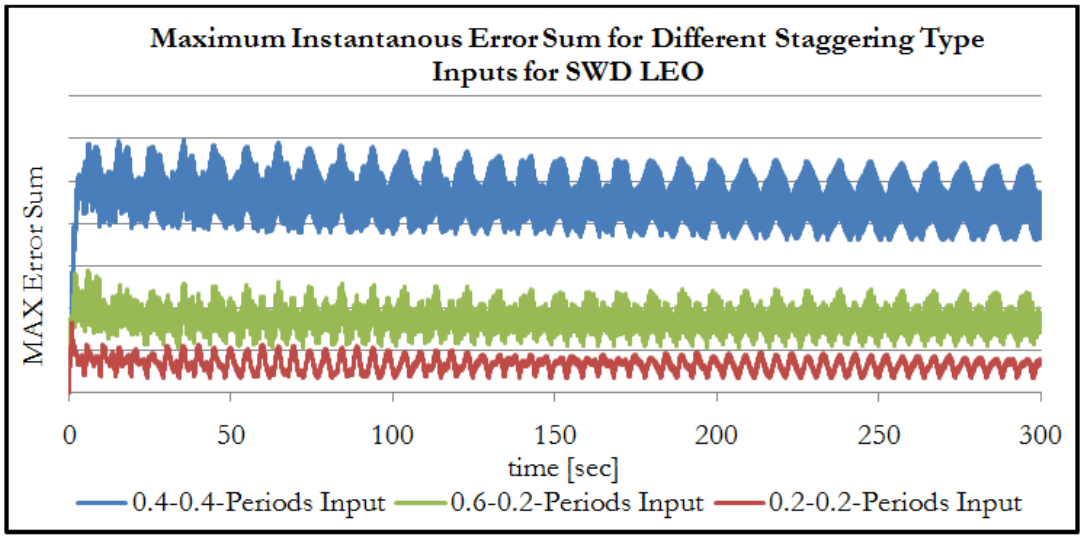

Figure 6.33 Maximum Instantaneous Error Sum under Different SWD GEO Inputs

The proposed 0.6-0.2-period and 0.2-0.2-period inputs exceptionally decrease the pointing error in the steady state region by 56% and 84% respectively. This is a superior achievement in reducing pointing error in the LEO orbit.

7. A NOVEL METHOD IN PERFORMING MODE-SUPERPOSITION TRANSIENT ANALYSIS USING MODAL EFFECTIVE MASSES

7.1 Motivation

Mode-superposition method is a method of using natural frequencies and mode shapes from the modal analysis to characterize the dynamic response of a structure to transient or steady harmonic excitations. Transient response using mode-superposition method is studied by Craig *et. al.* in [41] and by Huebner *et. al.* in [42]. Guo *et. al.* conduct a study on performing transient analysis of space frames using the method of reverberation-ray matrix and the orthogonality of normal modes in [43]. Hansteen and Bell studies the accuracy of mode superposition analysis in structural dynamics in [44].

In many practical applications it is very common that designers assume the first 10% or 20% of mode shapes to perform mode-superposition transient analysis; however, a better understanding of the concept of modal effective mass can be helpful when a mode-superposition approach is preferred to full method. The study conducted on a triangular lattice space structure with straight beams revealed that assuming fewer number of mode shapes, even first 1% in some cases, can still lead to obtaining an accurate transient response as long as the assumed mode shapes cover a large amount of modal effective masses in the directions of loadings.

Modal effective mass is a powerful tool in identifying the level of importance of mode shapes when there is a base excitation. As discussed before, modes having larger

modal effective masses contribute more in the transient response depending on the input. This became source of an idea to perform a mode-superposition transient analysis assuming the first few modes covering most of the total effective mass, 64% in this study, and compare obtained results with the common method of assuming first 10% of modes, which may or may not cover most of the total effective mass, and also with the results from the full method.

A triangular lattice space structure is generated in ANSYS to perform transient analysis using different methods under the same input. Results are compared to determine the efficacy of the proposed method based on modal effective mass concept. Material properties and dimension of the beams used in the present structure are the same as those used for the simple 3-beam frame model introduced previously for modal effective mass studies. The following picture shows the model of the lattice space structure used for mode-superposition transient studies.

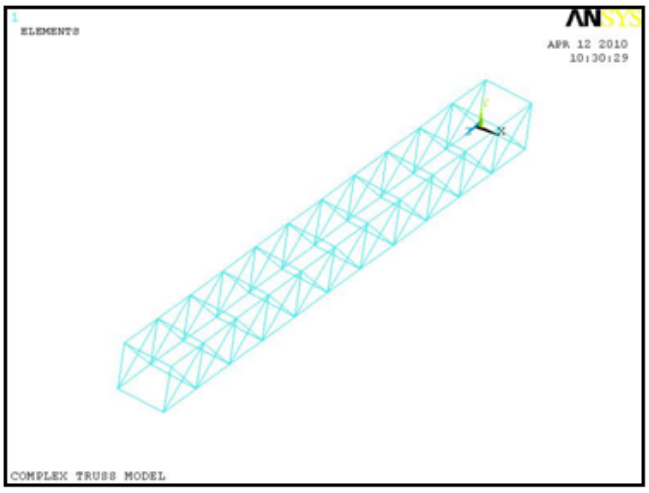

Figure 7.1 Triangular Lattice Space Structure for Mode-superposition Transient Studies

7.2 Modal Analysis

Modal analysis is performed assuming 200 modes to find the natural frequencies and modal effective masses. It is assumed that the base of the structure is grounded and therefore has no degrees of freedom. Results of natural frequencies and translational percent modal effective masses are summarized in the following table for the first 20 modes shapes.

Table 7.1 Modal Analysis Results of the Lattice Space Structure under Study

Mode	Freq [Hz]	%X	%Y	%Z
1	2.8	78.6	0	0
2	6.1	0	63.6	0
3	7.75	0	0	0
4	8.74	11.6	0	0
5	15.85	3.7	0	0
6	23.48	2	0	0
7	31.07	0	0	0
8	32.37	1.3	0	0
9	35.56	0	20.5	0
10	42.59	0.9	0	0

Mode	Freq [Hz]	%X	%Y	%Z
11	49.91	0	0	0
12	54.37	0.7	0	0
13	56.78	0	0	0
14	62.27	0	0	0
15	65.59	0	0	0
16	67.28	0.5	0	0
17	68.1	0	0	0
18	68.12	0	0	83.4
19	72.03	0	0	0
20	74.22	0	0	0
SUM		**99.4**	**84.1**	**83.4**

7.3 Transient Analysis under Full and Mode-superposition Methods

7.3.1 Excitation Input

A sinusoidal excitation force with frequency of 26 Hz and amplitude of 5 KN is assumed for the different transient analysis studies. The excitation input can be expressed as:

$$F_y = 5000 \sin(52\pi t) \quad N$$

The frequency of excitation force is chosen such that it does not equal, or very close, to any natural frequency of the structure; because in that case the excitation would excite only that specific mode shape which results in participating of only that mode in the transient response. The input is applied at the middle of the structure in the Y-direction. Furthermore, as the results from modal analysis show, in the Y-direction 63.6% of total effective mass is concentrated in the 2nd mode shape at 6.10 Hz and 20.5% in the 9th mode at 35.56 Hz.

7.3.2 Cases of Study

This study conducts 3 different scenarios of performing transient analysis and then compares the results obtained. Scenarios studied here are as follows:

- Full transient method (time-consuming method).
- Mode-superposition method assuming first 10% of modes, in this case first 20 modes (common method).

- Mode-superposition method assuming first 1% of modes, in this case first 2 modes covering 64% of total effective mass in the Y-direction (proposed method).

7.3.3 Comparison of Transient Displacement Responses

Transient UY displacement of a node on the tip of the structure is considered and plotted in a single graph below for all scenarios to determine accuracy of the proposed method.

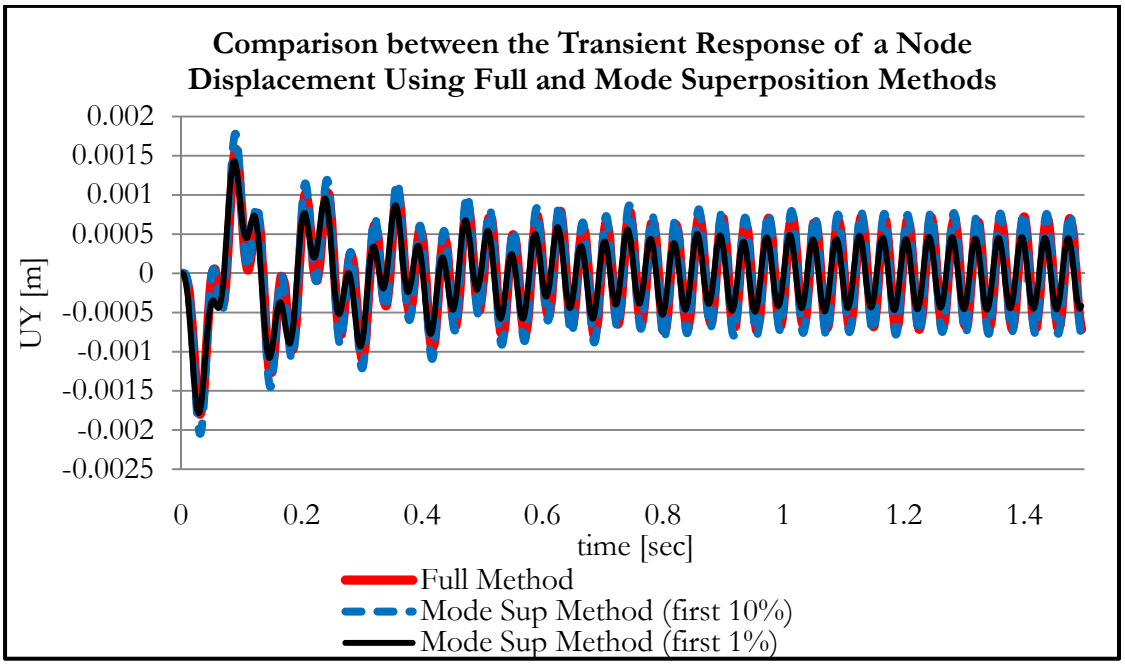

Figure 7.2 Comparison of Full and Mode-superposition Methods

Results show that mode-superposition method can be used assuming fewer number of mode shapes if a large amount of modal effective mass is considered. In this

case of study, since the 2nd mode covers 64% of total effective mass in the Y-direction, assumption of using the first two modes still leads to acceptable results. However, in more complex structures a larger number of mode shapes, and still less than first 10%, should be considered to cover a relatively large modal effective mass to perform mode-superposition transient analysis. Also in this case of study the processing time reduced by 21% using the proposed method compared the common method.

8. CONCLUSION

The results obtained from several studies and computer simulations meet the design requirements as discussed individually in each section.

The equivalent models developed through studies of modal analysis results showed a good correlation with the actual model results. This confirms that they can be used for further parametric studies.

The proposed input profiles for SWD GEO and LEO orbits exceptionally increased the dynamic performance of the structure. Several comparisons that are made between the new results under proposed inputs and the results under current design led to this conclusion that the proposed inputs can be used for higher energy generating performance considerations.

The novel method developed for performing mode-superposition transient analysis showed that assuming a smaller number of mode shapes can result in accurate results and there is no obligation on assuming first 10% or 20% of mode shapes to assure accurate results. This proved through a comparison between full transient analysis and mode-superposition transient analysis assuming first 10% and first 1% of the mode shapes.

REFERENCES

[1] John L. Junkins. *Mechanics and Control of Large Flexible Structures (Progress in Astronautics and Aeronautics).* Washington, DC : Amer Institutuion of Aeronautics and Astronautics, 1990.

[2] John L. Junkins and Youdan Kim. *Introduction to Dynamics and Control of Flexible Structures.* Washington, DC : AIAA (American Institute of Aeronautics & Astronautics), 1993.

[3] Colin L. Kirk and D. J. Inman. *Dynamics and Control of Structures in Space III.* Billerica, MA : Computational Mechanics Inc, 1996.

[4] Colin L. Kirk and John L. Junkins. *Dynamics of Flexible Structures in Space.* Southampton, UK : Computational Mechanics Publications, 1990.

[5] Bong Wie. *On the Modeling and Control of Flexible Space Structures.* Stanford, CA : Stanford University, 1981.

[6] Bong Wie. *Space Vehicle Dynamics and Control.* Reston, VA : American Institute of Aeronautics and Astronautics, 1952.

[7] Colin L. Kirk and John L. Junkins. *Dynamics of Flexible Structures in Space: Proceedings of the First International Conference, Cranfield, UK.* New York: Springer, 1990.

[8] Colin L. Kirk. *Dynamics and Control of Structures in Space II. in Proc. of the Second.* Washington, DC : Computational Mechanics Publications, 1993.

[9] V. V. Beletsky and E. M. Levin. *Dynamics of Space Tether Systems.* San Diego, CA: Amer Astronautical Society, 1993.

[10] Vitali M. Melnikov and Vladimir A. Koshelev. *Large Space Structures Formed by Centrifugal Forces.* Amesterdam, The Netherlands : Gordon and Breach Science Publishers, 1998.

[11] John Joseph Anagnost. *Control and Stabilization of Flexible Space Structures.* Berkeley, CA : Springer, 1989.

[12] Yoon-Gyeoung Sung. *Model Reduction and Robust Vibration Control of Flexible Space Structures.* Tuscaloosa, AL : University of Alabama, 1997.

[13] NASA. *Tubular Spacecraft Booms*, Mofett Field, CA : NASA, 1971.

[14] Rchard M. Beam. *On the Phenomenon of Thermoelastic Instability (Thermal Flutter) of Booms with Open Cross Section.* Mofett Field, CA : NASA, 1969.

[15] Stephen P. Timoshenko and James M. Gere. *Theory of Elastic Stability.* Mineola, NY : Dover Publications, 2009.

[16] Mario Como and Antonio Grimaldi. *Theory of Stability of Continuous Elastic Structures.* Boca Raton, FL : CRC Press, 1995.

[17] Earl A. Thornton and Yool A. Kim. *Thermally Induced Bending Vibrations of a Flexible Roll-Up Solar Array.* Journal of Spacecraft and Rockets, Vol. 30, No. 4, Pages 438-448, 1993.

[18] R. Gupta and K. Rao. *Instability of Laminated Composite Thin-Walled Open-Section Beams.* Bangalore, India : Compos Struct, Vol. 4, No. 4, Pages 299-313, 1985.

[19] R. Gupta and K. Rao. *Finite Element Analysis of Laminated Anisotropic Thin-walled Open-section Beams.* Coimbatore, India : Compos Struct, Vol. 7, No. 3, Pages 225-226, 1987.

[20] T. H. G. Megson. *Structural and Stress Analysis.* Butlington, MA : Arnold

Publishers, 2005.

[21] F. P. J. Rimrott. *Design Formulae for STEMs(TM).* Toronto : University of Toronto, Department of Mechanical Engineering, 1975.

[22] Jong-Hwi Seo, Jang-Soo Chae, Tae-Won Park, Sang-Won Han, Jang-Bom Chai and Hyun-Seok Seo. *Solar Panel Deployment Analysis of a Satellite System.* JSME International Journal, Vol. 46, No. 2, Pages 508-518, 2002.

[23] Oskar Wallrapp and Simon Wiedemann. *Simulation of Deployment of a Flexible Solar Array.* Berkeley, CA : Kluwer Academic Publishers, Vol. 7, No. 1, Pages 101-125, 2002.

[24] Oskar Wallrapp and Simon Wiedemann. *Comparison of Results in Flexible Multibody Dynamics Using Various Approaches.* Berkeley, CA : Kluwer Academic Publishers, Vol. 34, No. 1-2, Pages 189-206, 2003.

[25] Muthukrishnan Sathyamoorthy. *Nonlinear Analysis of Structures.* Boca Raton, FL : CRC Press, 1997.

[26] J. N. Reddy. *An Introduction to Nonlinear Finite Element Analysis.* New York : Oxford University Press, 2004.

[27] O. C. Zienkiewicz and R. L. Taylor. *The Finite Element Method: Volume 2, Solid Mechanics.* Oxford, UK : Butterworth-Heinemann, 2000.

[28] Thuc Phuong Vo and Jaehong Lee. *Geometrically Nonlinear Analysis of Thin-walled Open-section Composite Beams.* An International Journal of Computers and Structures, Vol. 88, No. 5-6, Pages 347-356, 2010.

[29] Thuc Phuong Vo and Joehong Lee. *Geometrically Nonlinear Theory of Thin-Walled Composite Box Beams Using Shear-deformable Beam Theory.* International Journal of Mechanical Science, Vol. 52, No. 1, Pages 65-74, 2010.

[30] Thuc Phuong Vo and Joehong Lee. *Geometrically Nonlinear Analysis of Thin-walled Composite Box Beams.* An International Journal of Computers and Structures, Vol. 87, No. 3-4, Pages 236-245, 2009.

[31] Clarence W. de. Silva. *Vibration: Fundamentals and Practice.* Boca Raton, FL : CRC Press, 2007.

[32] J. Wijker. *Spacecraft Structures.* Berkeley, CA : Springer, 2008.

[33] James F. Doyle. *Static and Dynamic Analysis of Structures: with an Emphasis on Mechanics and Computer Matrix Methods.* Norwell, MA : Kluwer Academic Publishers, 1991.

[34] Daniel Schiff. *Dynamic Analysis and Failure Modes of Simple Structures.* New York : Wiley-Interscience, 1990.

[35] O. Sergeyev and Z. Mroz. *Sensitivity Analysis and Optimal Design of 3D Frame Structures for Stress and Frequency Constraints.* Journal of Computers and Structures, Vol. 75, No. 2, Pages 167-185, 2000.

[36] William T. Thomson. *Theory of Vibration with Applications.* Cheltenham, England : Nelson Thornes Publishers, 1993.

[37] Leonard Meirovitch. *Fundamentals of Vibrations.* Boston : McGraw-Hill, 2001.

[38] M. G. Calkin. *Lagrangian and Hamiltonian Mechanics.* Singapore : World Scientific Publishing Co. Pte. Ltd., 2005.

[39] J. Kauppinen and J. Partanen. *Fourier Transforms in Spectroscopy.* Berlin, Germany : Wiley, 2001.

[40] C. Gasquet and P. Witomski. *Fourier Analysis and Applications: Filtering,*

Numerical, Computation, Wavelets. Ann Arbor, MI : Springer, 1999.

[41] Roy R. Craig and Andrew J. Kurdila. *Fundamentals of Structural Dynamics.* Hoboken, NJ : Wiley, 2006.

[42] Kenneth H. Huebner, Donald L. Dewhirst, Douglas E. Smith and Ted G. Byrom. *The Finite Element Method for Engineers.* New York : Wiley, 2001.

[43] Y. Q. Guo, W. Q. Chen and Y.-H. Pao. *Dynamic Analysis of Space Frames: The Method of Reverberation-ray Matrix and The Orthogonality of Mode Shapes.* Hangzhou, China : Journal of Sound and Vibration, Vol. 317, No. 3-5, Pages 716-736, 2008.

[44] C. Konke, R. Flesch and T. Wenk. *Earthquake Engineering and Structural Dynamics.* Berkeley, CA : Springer, 2010.

[45] ANSYS, Inc. *ANSYS Software Help Documanetation.* Canonsburg, PA : ANSYS Inc., 2009.

APPENDIX A

ANSYS ELEMENT DESCRIPTION

A.1 LINK10 Element

LINK10 is a 3-D spar element having the unique feature of a bilinear stiffness matrix resulting in a uniaxial tension-only (or compression-only) element. With the tension-only option, the stiffness is removed if the element goes into compression (simulating a slack cable or slack chain condition). This feature is useful for static guy-wire applications where the entire guy wire is modeled with one element. It may also be used in dynamic analyses (with inertia or damping effects) where slack element capability is desired but the motion of the slack elements is not of primary interest [45].

LINK10 has three degrees of freedom at each node: translations in the nodal x, y, and z directions. No bending stiffness is included in either the tension-only (cable) option or the compression-only (gap) option but may be added by superimposing a beam element with very small area on each LINK10 element. Stress stiffening and large deflection capabilities are available [45]. The geometry, node locations, and the coordinate system for this element are shown below.

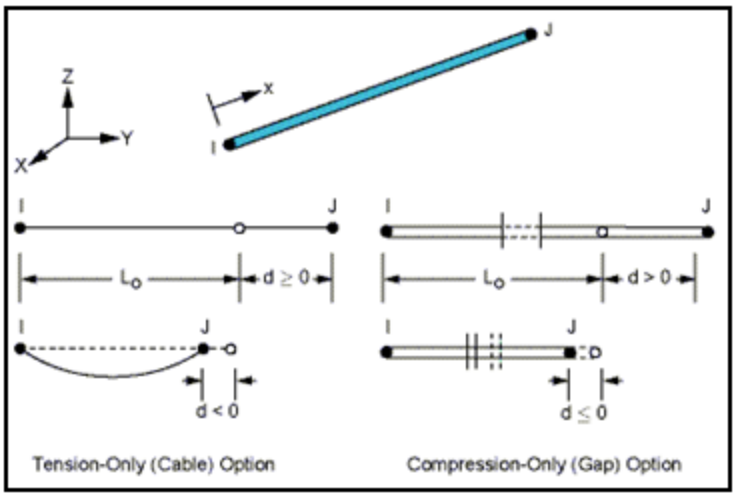

Figure A.1 LINK10 Geometry

The element is defined by two nodes, the cross-sectional area, an initial strain or gap, and the isotropic material properties. The element x-axis is oriented along the length of the element from node I toward node J [45].

The initial strain in the element (ISTRN) is given by Δ/L, where Δ is the difference between the element length, L, (as defined by the I and J node locations) and the zero strain length, Lo. For the cable option, a negative strain indicates a slack condition. For the gap option, a positive strain indicates a gap condition. The gap must be input as a "per unit length" value [45].

A.2 BEAM4 Element

BEAM4 is a uniaxial element with tension, compression, torsion, and bending capabilities. The element has six degrees of freedom at each node: translations in the nodal x, y, and z directions and rotations about the nodal x, y, and z axes. Stress

stiffening and large deflection capabilities are included. A consistent tangent stiffness matrix option is available for use in large deflection (finite rotation) analyses [45]. The geometry, node locations, and coordinate systems for this element are shown below.

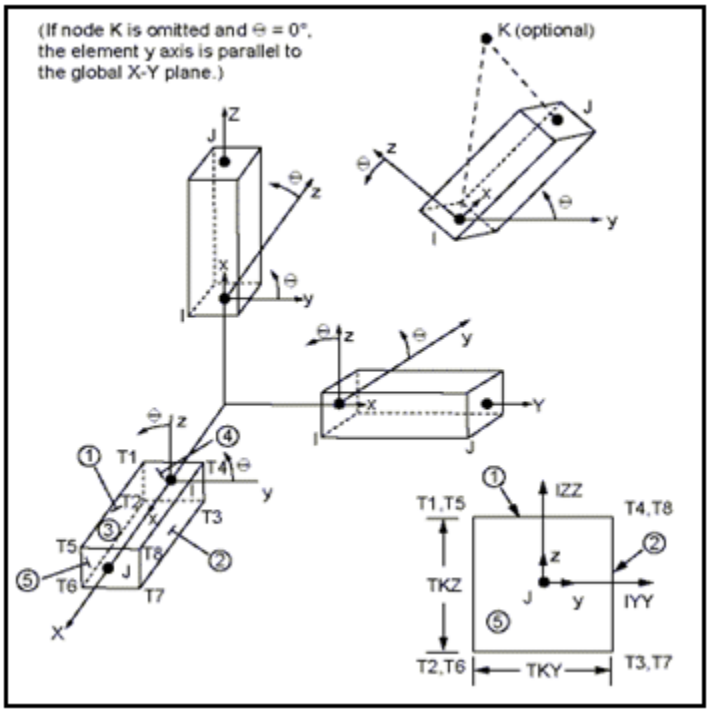

Figure A.2 BEAM4 Geometry

The element is defined by two or three nodes, the cross-sectional area, two area moments of inertia (IZZ and IYY), two thicknesses (TKY and TKZ), an angle of orientation (θ) about the element x-axis, the torsional moment of inertia (IXX), and the material properties [45].

The initial strain in the element (ISTRN) is given by Δ/L, where Δ is the difference between the element length, L, (as defined by the I and J node locations) and

the zero strain length. The shear deflection constants (SHEARZ and SHEARY) are used only if shear deflection is to be included. A zero value of SHEAR_ may be used to neglect shear deflection in a particular direction [45].

A.3 BEAM188 Element

BEAM188 is suitable for analyzing slender to moderately stubby/thick beam structures. This element is based on Timoshenko beam theory. Shear deformation effects are included. BEAM188 is a linear (2-node) or a quadratic beam element in 3-D. BEAM188 has six or seven degrees of freedom at each node, with the number of degrees of freedom depending on the value of KEYOPT(1). When KEYOPT(1) = 0 (the default), six degrees of freedom occur at each node. These include translations in the x, y, and z directions and rotations about the x, y, and z directions. When KEYOPT(1) = 1, a seventh degree of freedom (warping magnitude) is also considered. This element is well-suited for linear, large rotation, and/or large strain nonlinear applications [45].

BEAM188 includes stress stiffness terms, by default. The provided stress stiffness terms enable the elements to analyze flexural, lateral, and torsional stability problems (using eigenvalue buckling or collapse studies with arc length methods) [45].

Elasticity, creep, and plasticity models are supported (irrespective of cross-section subtype). A cross-section associated with this element type can be a built-up section referencing more than one material [45].

The geometry, node locations, and coordinate system for this element are shown below.

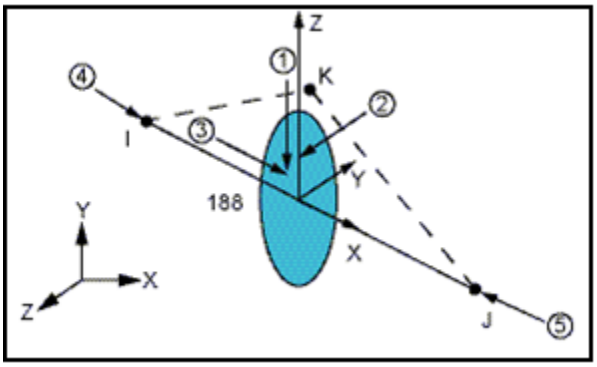

Figure A.3 BEAM188 Geometry

BEAM188 is defined by nodes I and J in the global coordinate system. Node K is a preferred way to define the orientation of the element.

VITA

Name:	Navid Mohsenizadeh
Address:	Texas A&M University Department of Mechanical Engineering 3123 TAMU College Station, TX 77843-3123
Email Address:	navidm@tamu.edu
Education:	B.S., Mechanical Engineering, Shiraz University, 2007 M.S., Mechanical Engineering, Texas A&M University, College Station, TX, 2010